A NOVEL APPROACH TO MINERAL CARBONATION: ENHANCING CARBONATION WHILE AVOIDING MINERAL PRETREATMENT PROCESS COST

Type of Report:	Annual
Reporting Period Start Date:	June 22, 2005
Reporting Period End Date:	June 21, 2006
Principal Authors:	Michael J. McKelvy,* Andrew V.G. Chizmeshya, Kyle Squires, Ray W. Carpenter, and Hamdallah Béarat.
Date Report Issued:	November 2006
DOE Award Number:	DE-FG26-04NT42124
Submitting Organization:	Arizona State University Center for Solid State Science, Science and Engineering of Materials Graduate Program, and Department of Mechanical and Aerospace Engineering Tempe, AZ 85287-1704 * Phone: (480) 965-4535; FAX: (480) 965-9004; E-mail: mckelvy@asu.edu

DISCLAIMER

ABSTRACT

Known fossil fuel reserves, especially coal, can support global energy demands for centuries to come, ***if*** the environmental problems associated with CO_2 emissions can be overcome. Unlike other CO_2 sequestration candidate technologies that propose long-term storage, mineral sequestration provides permanent disposal by forming geologically stable mineral carbonates. Carbonation of the widely occurring mineral olivine (e.g., forsterite, Mg_2SiO_4) is a large-scale sequestration process candidate for regional implementation, which converts CO_2 into the environmentally benign mineral magnesite ($MgCO_3$). The primary goal is cost-competitive process development. As the process is exothermic, it inherently offers low-cost potential. Enhancing carbonation reactivity is key to economic viability. Recent studies at the U.S. DOE Albany Research Center have established that aqueous-solution carbonation using supercritical CO_2 is a promising process; even without olivine activation, 30-50% carbonation has been achieved in an hour. Mechanical activation (e.g., attrition) has accelerated the carbonation process to an industrial timescale (i.e., near completion in less than an hour), at reduced pressure and temperature. However, the activation cost is too high to be economical and lower cost pretreatment options are needed. Herein, we report our second year progress in exploring a novel approach that offers the potential to substantially enhance carbonation reactivity while bypassing pretreatment activation. As our second year progress is intimately related to our earlier work, the report is presented in that context to provide better overall understanding of the progress made.

We have discovered that robust silica-rich passivating layers form on the olivine surface during carbonation. As carbonation proceeds, these passivating layers thicken, fracture and eventually exfoliate, exposing fresh olivine surfaces during rapidly-stirred/circulating carbonation. We are exploring the mechanisms that govern carbonation reactivity and the impact that (i) modeling/controlling the slurry fluid-flow conditions, (ii) varying the aqueous ion species/size and concentration (e.g., Li^+, Na^+, K^+, Rb^+, Cl^-, HCO_3^-), and (iii) incorporating select sonication offer to enhance exfoliation and carbonation. We have succeeded in nearly doubling the extent of carbonation observed compared with the optimum procedure previously developed by the Albany Research Center. Aqueous carbonation reactivity was found to be a strong function of the ionic species present and their aqueous activities, as well as the slurry fluid flow conditions incorporated. High concentration sodium, potassium, and sodium/potassium bicarbonate aqueous solutions have been found to be the most effective solutions for enhancing aqueous olivine carbonation to date. Slurry-flow modeling using Fluent indicates that the slurry-flow dynamics are a strong function of particle size and mass, suggesting that controlling these parameters may offer substantial potential to enhance carbonation. Synergistic control of the slurry-flow and aqueous chemistry parameters offers further potential to improve carbonation reactivity, which is being investigated during the no-cost extension period.

During the first project year we developed a new sonication exfoliation system with a novel sealing system to carry out the sonication studies. We also initiated investigations into the potential that sonication offers to enhance carbonation reactivity. During the second project year, we extended our investigations of the effects of sonication on the extent of carbonation as a function of the following parameters: particle size distribution, the mass of solid reactant, volume fraction of aqueous solution present, sonication power, time, temperature, and CO_2 pressure. Thus far, none of the conditions investigated have significantly enhanced carbonation.

Mechanistic investigations of the stirred (~1,500 rpm) aqueous olivine carbonation process indicate the carbonation process involves both incongruent magnesium dissolution and silica precipitation, which results in robust silica-rich passivating layer formation. Secondary ion mass spectrometry observation of H within the passivating layer that forms during static carbonation suggests $2H^+/Mg^{2+}$ ion exchange is associated with incongruent dissolution. Apparently, H_2O forms at or near the olivine/passivating-layer

interface during the process and diffuses out through the passivating layers during the carbonation reaction. This is also consistent with the observation that magnesite nanocrystals form within the passivating layers, further indicating the layers offer significant permeability to the key solution reaction species present during carbonation (e.g., Mg^{2+}, H^{+}, H_2O, CO_2, and HCO_3^{-}). Cracking of the passivating layer surface during carbonation is routinely observed and can be related to the tensile stress associated with the dramatic volume decrease as olivine forms silica at the reaction surface. The addition of quartz particles as an abrasive slurry component significantly enhanced carbonation, further substantiating the importance of particle-particle abrasion in enhancing passivating layer exfoliation and carbonation. Studies during the no-cost extension period will emphasize the impact that controlled aqueous speciation and activity and slurry-flow dynamics have on the mechanisms that control carbonation reactivity and the potential they offer to substantially reduce olivine mineral sequestration process cost.

TABLE OF CONTENTS

Title Page 1

Disclaimer 2

Abstract 3

Table of Contents 5

Executive Summary 6

Introduction 8

Experimental 9

Results and Discussion 10

Conclusions 43

References 44

Appendix (*Environmental Science & Technology* **2006,** 40, 4802-8)..... 45

EXECUTIVE SUMMARY

CO_2 mineral sequestration provides permanent carbon dioxide disposal by forming geologically stable and environmentally benign mineral carbonates. Carbonation of olivine (e.g., forsterite, Mg_2SiO_4) is a large-scale sequestration process candidate for regional implementation. Cost-effectively enhancing carbonation reactivity is central to economically viable process development. Aqueous-solution carbonation shows particular promise. However, the associated mineral activation cost currently needed to suitably enhance carbonation is too high. Lower cost pretreatment options are needed. During the second year of this project, we have continued to explore the potential to substantially enhance carbonation reactivity via a novel approach that bypasses pretreatment activation altogether. As our second year progress is intimately related to our earlier work, the report is presented in that context to provide better overall understanding of the progress made.

We have discovered that silica-rich passivating layers form on the olivine surface during carbonation. The process appears to be associated with both incongruent olivine dissolution (i.e., preferential magnesium dissolution) and silica precipitation, which together lead to the formation of the robust silica-rich passivating layers that form. During carbonation, the layers thicken, fracture and exfoliate during rapidly-stirred/circulating carbonation. This project is exploring the potential to cost-effectively enhance carbonation, while avoiding the cost of olivine pretreatment activation. Three approaches are being targeted: (i) controlling the aqueous chemistry (e.g., Li^+, Na^+, K^+, Rb^+, Cl^-, and HCO_3^- activities), (ii) integration of slurry flow modeling with experiment, and (iii) incorporating select sonication. The focus of these studies is on (1) mitigating passivating layer effectiveness, (2) enhancing exfoliation and (3) enhancing carbonation. We have succeeded in nearly doubling the extent of carbonation compared with that observed for the optimum procedure previously developed by the Albany Research Center (ARC).

During the first year, we discovered carbonation reactivity is a complicated function of the aqueous solution species/activities. Varying the aqueous alkali cation species in the optimum solution developed by the ARC (0.64M $NaHCO_3$ + 1.00M NaCl) found that the alkali cation species present and their ratio dramatically impact carbonation reactivity, with up to a factor of 20 difference in the extent of carbonation observed. High concentrations of $NaHCO_3$ and $KHCO_3$ were discovered to be particularly effective at enhancing carbonation. During the second year, we extended our investigations to explore the extent of carbonation vs. Na and K bicarbonate concentration, the Na/K ratio associated with the bicarbonate, temperature, and CO_2 pressure. Carbonation was found to increase with increasing Na and K bicarbonate concentration until very high concentrations, where it begins to decrease. The optimum concentrations for $NaHCO_3$ and $KHCO_3$ were found to be ~2.5M and ~5.5M, respectively, with higher concentrations resulting in lower extents of carbonation. This is consistent with initial solubility simulations that suggest that decreasing carbonation at very high bicarbonate concentrations may be associated with decreasing CO_2 solubility with increasing bicarbonate concentrations. Carbonation was observed to continuously increase with increasing CO_2 pressure, while an optimum temperature of 185 ^oC was observed below and above which the carbonation decreased. Alkali chloride solutions were further investigated in combination with high concentration Na, K, and Na/K bicarbonate solutions, partially motivated by the initial success of the ARC standard solution (0.64M $NaHCO_3$ + 1.00M NaCl). However, none of these aqueous solutions were as effective as the high concentration bicarbonate solutions. CO_2(aq), Na^+ and/or K^+, and HCO_3^- play key synergistic roles in enhancing carbonation, as carbonation drops off dramatically in the presence of Na^+/K^+ + HCO_3^-(aq) or CO_2(aq) alone.

During the first project year, multi-phase fluid modeling and experimental investigations were initiated to elucidate important slurry-flow parameters that enhance exfoliation and carbonation (e.g., via particle-particle and particle-wall collisions). A new, well validated, microscopic wall roughness model was developed. Simulations indicated wall roughness can strongly enhance cross-stream transport, particle

collisions and carbonation. The Fluent code was validated for application to multiphase flows to assess the complex effects governing flow and initially applied to components of the ARC flow-loop reactor. Results indicate the radial flow distribution in a component pipe can be a strong function of particle mass/size distribution and mixing history. Particle mass and carbonation flow characteristics were found to be important factors in carbonation reactivity, with the ASU batch reactor showing markedly enhanced carbonation in comparison with the ARC flow-loop reactor for <150 μ Twin Sisters olivine. As a result, during the second year of this project we have focused our simulation efforts on the simpler ASU batch reactor, which provides the critical advantage of being able to simulate the multiphase fluid flow for the whole system. This allows direct connection with experimental observations as we seek to utilize our simulations to control the multiphase fluid flow dynamics to enhance particle-particle and particle-reactor passivating-layer abrasion and carbonation. Initial whole system simulations as a function of particle size indicate it can dramatically impact both the particle concentration profile and velocity vectors, key factors that can substantially impact particle-particle abrasion, exfoliation, and carbonation. These studies, and complimentary experimental studies, are continuing during the no-cost extension.

A controlled pressure and temperature 20 kHz sonication system was successfully developed for these studies during the first year. During the second year the system was refined to utilize an improved sonic probe design that substantially extends the lifetime of the probe. During the second year, the system has been utilized to explore the effects of sonication on the extent of carbonation as a function of the weight % olivine present, particle size distribution, volume fraction of aqueous solution present, and sonication power, time, temperature, and CO_2 pressure. None of the conditions investigated significantly enhanced carbonation. As sonication is energy intensive, we have refocused our efforts to deepen our studies of the effects that aqueous solution chemistry and multiphase fluid flow can have on carbonation reactivity, as they offer the greatest promise for cost-effectively enhancing aqueous olivine carbonation.

Mechanistic investigations have extended the fundamental understanding of the passivating layer formation process during the second project year, with many of these results discussed in our recently published article "Carbon Sequestration via Aqueous Olivine Mineral Carbonation: Role of Passivating Layer Formation," in *Environmental Science and Technology (2006).* These investigations indicate both incongruent magnesium dissolution and silica precipitation contribute to silica-rich passivating layer formation. Secondary ion mass spectrometry observations of the hydrogen concentration within the passivating layer suggests $2H^+/Mg^{2+}$ ion exchange occurs in association with incongruent dissolution. In the process, H_2O forms in the olivine/passivating-layer interface region and diffuses out through the layers. Internal passivating-layer diffusion of key reaction species is also consistent with our observation of magnesite nanocrystals having formed within the passivating layers. Thus, during carbonation the layers have significant permeability to key reaction species such as Mg^{2+}, H^+, H_2O, CO_2, and HCO_3^-.

Cracking of the passivating layer surface during carbonation is routinely observed during both static and stirred investigations. This is related to the tensile stress at the interface between the silica-rich passivating layer and the underlying olivine host, due to the large volume reduction as the silica forms from its olivine host. The impact of abrasion on passivating layer exfoliation and carbonation was investigated via the addition of significant weight fractions of similarly sized quartz particles as an abrasive slurry. This process significantly enhanced carbonation under otherwise identical conditions, further substantiating the importance of particle-particle abrasion as a pathway for enhancing both passivating layer exfoliation and carbonation. Studies during the no-cost extension period will emphasize the impact that controlled aqueous speciation and activity and slurry-flow dynamics have on the mechanisms that control carbonation reactivity, as they offer the greatest potential to substantially reduce olivine mineral sequestration process cost.

INTRODUCTION

Fossil fuels are well positioned to supply the world's energy needs for centuries to come if carbon sequestration technology can be developed that is (i) permanent, (ii) environmentally benign, and (iii) economically viable.[1] CO_2 mineral sequestration provides permanent disposal, by forming geologically stable mineral carbonates.[2-5] The materials produced are also environmentally benign and found in vast quantities in nature. The primary challenge is economically viable process development. As permanent disposal inherently avoids the ongoing monitoring, remediation and liability costs associated with long-term storage, the key is reducing mineral sequestration process cost. Cost effectively enhancing carbonation reactivity is critical. Enhancing mineral carbonation during geological (below-ground) sequestration is highly desirable as well, as it can similarly ensure long-term sequestration stability via the formation of thermodynamically stable mineral carbonates.[6] Investigating and evaluating candidate technologies that incorporate mineral sequestration (above and below ground) is the primary focus of the CO_2 Mineral Sequestration Working Group, which is managed by DOE (Fossil Energy), and consists of members from the Albany Research Center, Argonne National Laboratory, Arizona State University, Los Alamos National Laboratory, and the National Energy Technology Laboratory.

Above ground carbonation of Mg-rich olivine minerals (e.g., forsterite, Mg_2SiO_4) is a leading mineral sequestration process candidate.[7,8] These minerals are available worldwide in quantities sufficient to support the regional implementation of above-ground mineral sequestration.[8] Their low-cost (~$4-5/ton for mined and milled feedstock)[7,8] and exothermic carbonation (reaction 1), provide the potential for economically viable process development.

(1) $\frac{1}{2}Mg_2SiO_4 + CO_2 \rightarrow MgCO_3 + \frac{1}{2}SiO_2 + 88$ kJ/mol

Recent studies at the Albany Research Center indicate aqueous solution carbonation is a promising approach.[7,8] Even without special activation, 30-50% carbonation has been achieved in an hour for <37 micron olivine reacted at 185 ^oC and 150 bar CO_2. Mechanical pretreatment via intense attrition accelerates carbonation to near completion in less than an hour and at reduced pressures and temperatures. However, the activation cost is too high for cost-effective sequestration.[8]

Economically viable process development will require novel approaches that enhance mineral carbonation reactivity, while bypassing costly mineral pretreatment. The potential to develop low-cost chemical pretreatment processes has been explored for years, but success remains elusive.[6] Enhancing carbonation, while avoiding the expense of olivine pretreatment, would substantially reduce process cost and provide a significant advance. We recently discovered that aqueous olivine mineral carbonation is associated with robust passivating layer formation, which substantially inhibits mineral carbonation. Herein, we are exploring novel low-cost approaches with the potential to mitigate passivating layer effectiveness, enhance carbonation and develop an atomic level understanding of the associated mechanisms. The goal is to develop the understanding needed to engineer new low-cost carbonation processes that avoid the cost of pretreatment activation. The primary focus is on mitigating passivating layer effectiveness, e.g.,

by enhancing exfoliation processes that expose fresh olivine surfaces, an approach with the potential to substantially enhance carbonation while avoiding the need for and cost of olivine pretreatment activation.

EXPERIMENTAL

Single crystal olivine fragments from San Carlos, Arizona, were used to explore the effects of aqueous solution chemistry, particle size and sonication on olivine carbonation reactivity, as well as the mechanisms that govern passivating layer formation and exfoliation processes. The elemental composition was determined to be $(Mg_{0.915}Fe_{0.085})_2SiO_4$ by electron microprobe and particle induced X-ray emission analysis. X-ray diffraction (XRD) of powdered samples showed the lattice constants are in good agreement with those observed for olivine containing ~8% Fe (a = 4.763Å, b = 10.223Å, c = 5.993Å).[9,10] Trace impurities observed were well below 1%, with Ca being the principle trace impurity. Single crystals and single crystal fragments were used to facilitate microscopic observation of passivating layer formation/exfoliation and the reaction surfaces and interfaces that form during carbonation. Synthetic forsterite (Mg_2SiO_4) (99% Mg_2SiO_4; Alfa Aesar) was used for select carbonation investigations. Twin Sisters olivine was used for the flow-loop reactor studies carried out in collaboration with the Albany Research Center.[7] The flow-loop reactor has been previously described.[8] All of the olivine size fractions investigated herein (<37 micron, 37-75 micron, < 75 micron, 75-150 micron and <150 micron) were wet screened. The extent of carbonation observed is compared with the optimum process to date for enhancing carbonation developed by the Albany Research Center (ARC),[7,8] which is summarized below for forsterite carbonation.

$$Mg_2SiO_4 + 2CO_2 \xrightarrow[0.64\ M\ NaHCO_3,\ 1M\ NaCl]{\sim 185\ ^\circ C,\ \sim 150\ atm\ CO_2} 2MgCO_3 + SiO_2$$

Reactions were carried out using a variety of aqueous species (e.g., Li^+, Na^+, K^+, Rb^+, Cl^-, HCO_3^-) and species activities, particle size ranges and reaction times to probe their effect on carbonation and passivating layer formation/exfoliation. 1,500 rpm stirring was used to replicate the ARC process in the studies at Arizona State University. These mineral carbonation reactions were performed using a 100ml Autoclave Engineers EZE-Seal Hastelloy C-276 reactor, which is a smaller scale version of the 2,000 ml EZE-Seal Hastelloy C-276 reactor used at the Albany Research Center. Unstirred (static) experiments were undertaken to explore passivating layer formation in the absence of particle abrasion. San Carlos olivine single crystals (~1x1x0.1cm) with well-defined initial surface orientations were incorporated to follow the reaction interface that forms down to the atomic level.

The extent of carbonation and hydrogen content of the product materials were assessed using a Perkin Elmer Series II CHNS Elemental Analyzer. Comparative standards gave total carbon and hydrogen accuracies of ± 0.3 wt%. Extent of carbonation observations were compared with XRD intensity analysis of the product materials and found to be in good agreement. Select reaction products were analyzed structurally, morphologically, and analytically versus their extent of reaction to probe the mechanisms that govern carbonation.

XRD patterns were obtained using a Rigaku D/MAX-IIB X-ray diffractometer with Cu$K\alpha$ radiation. Scans were taken over different 2θ ranges between 10º to 70º, with 0.01º/s steps.

Reaction products were imaged using a Hitachi S-4700 field-emission scanning electron microscope (FESEM) or a FEI XL-30 Environmental FESEM. Elemental analysis of individual product particles was accomplished via energy dispersive X-ray spectroscopy (EDS). Cross-sectioned samples of reaction interfaces were analyzed via FESEM and EDS mapping and high-resolution transmission electron microscopy (HRTEM) using a JEOL 2010 with EDS and electron energy loss spectroscopy (EELS) capabilities. Secondary ion mass spectrometry (SIMS) analyses were performed using a spectrometer (Model3f, CamecaIMS, Courbevoie, France).

Controlled pressure and temperature studies of the impact of sonication on olivine exfoliation/carbonation were carried out using our batch mineral carbonation reaction system described above and our specially developed controlled pressure and temperature sonication system described below. Sonication/carbonation studies have been carried out in stages. Hour-long carbonation studies are separated into three stages: (1) a half hour long run in the batch reactor, followed by (2) controlled sonication in the sonication system (e.g., one minute) and (3) a second half hour in the batch reactor. The above sonication runs are compared to both the standard one-hour carbonation runs using the batch reactor and runs that incorporate the sonication reaction stages (1/2 hour plus 1/2 hour batch reaction format), but without sonication.

RESULTS AND DISCUSSION

Technical Accomplishments: Enhancing the Sonic Exfoliation System

During the first project year we developed a controlled pressure and temperature 20 kHz sonication system for these studies. The system is based on a Sonics 1500 watt power supply and a special probe to adapt to our custom controlled pressure (1 to 200 atm) and temperature (20 to 250 ^{o}C) sonication vessel. The pressure and temperature control system used is the same system used to conduct our aqueous carbonation reactions. The impeller driven stirring system is replaced by the sonic probe. Other than the interchangeable sonication and impeller components, the remainder of the system remains essentially the same. During the second year, the sonic probe failed prematurely, and it became apparent that the design of the probe needed to be modified. The design was refined and improved in collaboration with Sonics Inc. based on the failure mode for the first generation of probes. The new design has substantially extended the life of the probe and has been utilized for the second year sonication studies described below.

Scientific Progress: Effects of Aqueous Chemical Speciation and Activity on Olivine Carbonation Reactivity.

We are investigating the effect of aqueous solution species/activity on extent of carbonation using our 100 ml batch carbonation reaction system. The extent of carbonation observed for these investigations is compared with that observed using the optimum conditions to enhance carbonation developed by the ARC, which incorporates an aqueous solution of 0.64M $NaHCO_3$ + 1.00 M NaCl, and 1 hour reaction time at 185 ^{o}C, under 2200 psi of CO_2, with ~ 1500rpm stirring. <38μ San Carlos olivine (essentially single crystal fragments) was used for the comparative studies. The objective of these investigations is to further evaluate (i) the effect of

aqueous chemical speciation and concentration on olivine passivating layer formation and carbonation reactivity and (ii) the potential controlling them offers to enhance carbonation. During the second project year the primary focus has been on the effect of the activities of the alkali cation, chloride and bicarbonate species present. As substantial increases in the extent of carbonation were observed using higher concentration Na/K bicarbonate solutions, our studies have emphasized a thorough exploration of the potential these solutions offer to enhance carbonation as a function of their activity, Na/K ratio, and the associated reaction temperature and pressure (P_{CO2}). All results are compared to the extent of carbonation observed using the standard 0.64M $NaHCO_3$ + 1.0 M NaCl aqueous solution developed at the Albany Research Center (ARC).[7] Other than varying the above parameters, the impact of which are the primary focus of these studies, the other conditions associated with the optimum procedure developed by the ARC were used throughout. The carbonation extents reported are calculated based on elemental carbon analysis of the product materials, which are semi-quantitatively verified via X-ray powder diffraction analysis. All of the product carbonate formed herein is identified as magnesite.

1. Exploring the Potential that Potassium/Sodium Bicarbonate Solutions Offer to Enhance Aqueous Olivine Carbonation Reactivity

High aqueous bicarbonate concentrations were observed to substantially enhance olivine carbonation reactivity in comparison with the standard ARC 0.64M $NaHCO_3$ + 1.00 M NaCl aqueous solution. In order to more fully explore the potential high aqueous bicarbonate concentrations offer to enhance carbonation reactivity, we investigated the carbonation reactivity associated with $NaHCO_3$ and $KHCO_3$ solutions as a function of their aqueous concentration and Na/K ratio. Plots of extent of carbonation versus [$NaHCO_3$] and [$KHCO_3$] are shown in Figures 1 & 2 below. A strong increase in carbonation extent is observed with increasing bicarbonate concentrations for both sodium and potassium bicarbonate, which peaks at relatively high bicarbonate concentrations and begins to decrease at still higher bicarbonate concentrations. The peak extent of carbonation is ~2.5M for $NaHCO_3$ and ~5.5M for $KHCO_3$. Aqueous solutions containing CO_2(aq) and Na^+ or K^+, and HCO_3^- have provided the best synergistic combination of solution ions for enhancing mineral carbonation to date, nearly doubling the extent of carbonation observed using the standard ARC solution. It is interesting to note the strong positive effect that Na^+ has on carbonation in comparison with similar concentrations of K^+, highlighting the important role that cation species can play in carbonation. It is also important to note that further increasing the bicarbonate concentration eventually leads to lower carbonation extents.

If the above effect were simply associated with reaching the solubility limit of $NaHCO_3$ and $KHCO_3$ at 185 ^oC and 150 atm CO_2, the extent of carbonation might be expected to reach a plateau at the highest bicarbonate concentrations, with any further bicarbonate that is added simply remaining in solid form. Instead, the extent of carbonation decreases significantly for increasingly high Na/K bicarbonate concentrations, which may be associated with decreasing CO_2 solubility with increasing ionic Na/K bicarbonate concentrations. This hypothesis is

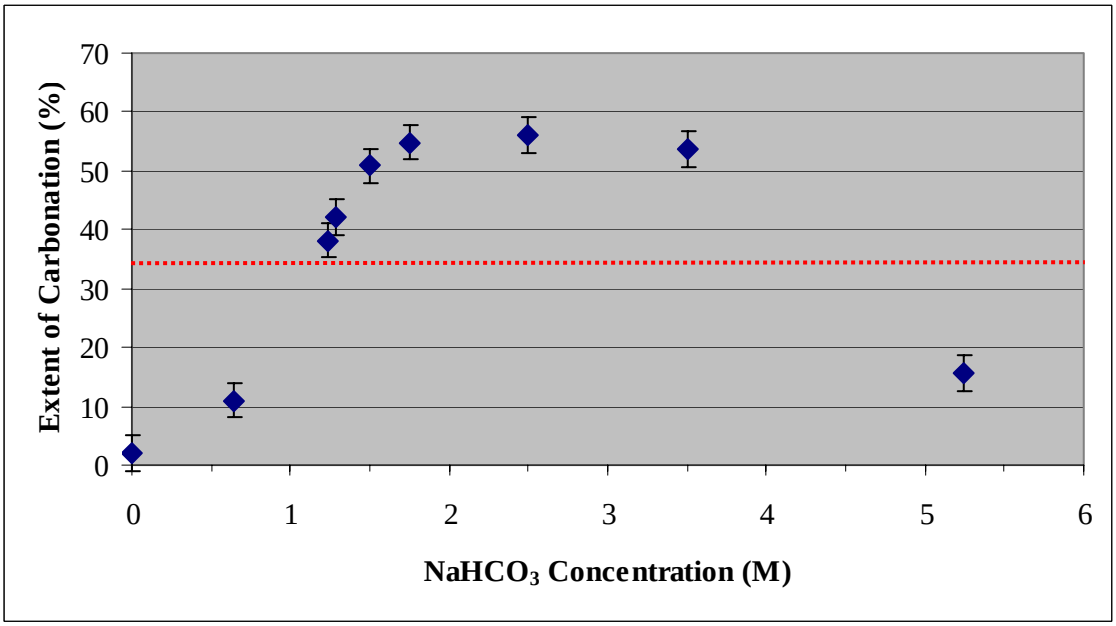

Figure 1: *Extent of carbonation of < 38 µ San Carlos Olivine as a function of $NaHCO_3$ concentration after 1h of carbonation at 185°C, under 2200psi of CO_2, and with ~1500rpm stirring. The dashed horizontal red line represents the extent of carbonation observed using the standard 0.64M $NaHCO_3$ + 1.00 M NaCl aqueous solution under the same reaction conditions.*

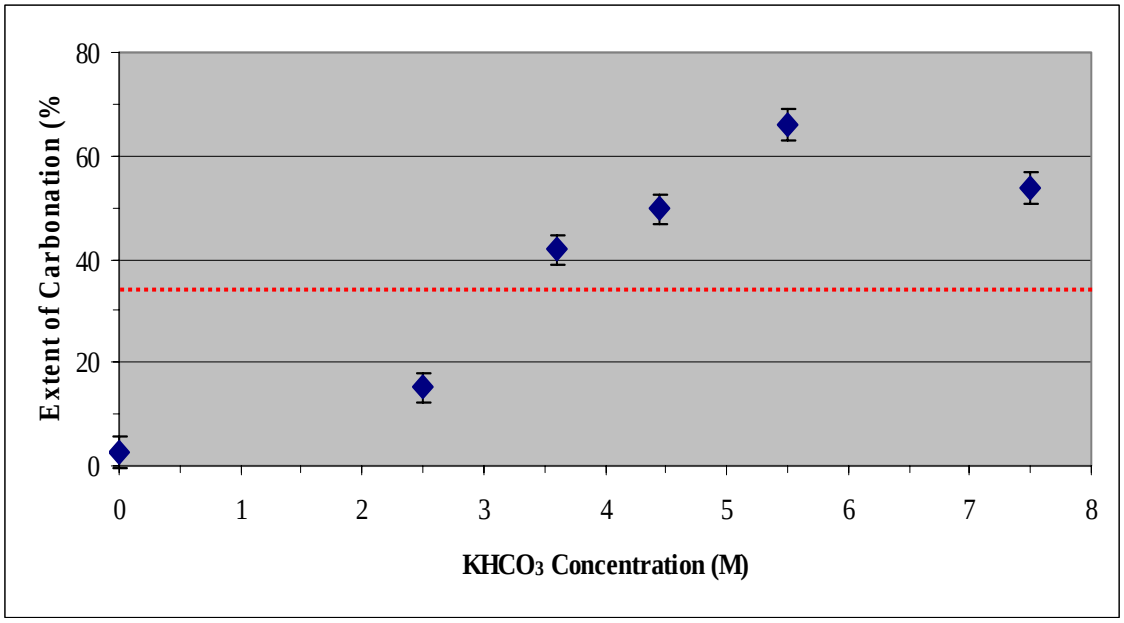

Figure 2: *Extent of carbonation of < 38 µ San Carlos Olivine as a function of $KHCO_3$ concentration after 1h of carbonation at 185°C, under 2200psi of CO_2, and with ~1500rpm stirring. The dashed horizontal red line represents the extent of carbonation observed using the standard 0.64M $NaHCO_3$ + 1.00 M NaCl aqueous solution under the same reaction conditions.*

consistent with previous simulations that indicate that increasing ionic NaCl concentrations may significantly reduce aqueous CO_2 solubility (see below). Future NMR probe and simulation investigations are planned to explore the effect of increasing Na/K bicarbonate concentrations on CO_2 solubility to assess the extent to which the above decrease in carbonation extent may be related to decreasing aqueous CO_2 solubility at very high bicarbonate concentrations.[11,12]

We have previously observed that using mixtures of $NaHCO_3$ and $KHCO_3$ and varying the Na^+/K^+ ratio can significantly improve the extent of olivine carbonation when starting with the standard solution of 0.64M $NaHCO_3$ + 1.00 M NaCl, as seen in Figure 3. This led us to explore the potential for further enhancing carbonation reactivity by varying the Na^+/K^+ ratio for high bicarbonate concentrations [i.e., 2.5 M $(Na/K)HCO_3$]. As seen in Figure 4, the Na^+/K^+ ratio has a dramatic impact on carbonation reactivity. The extent of carbonation dramatically increases with increasing Na^+/K^+ ratio, but does not exceed the value observed for 2.5 M $NaHCO_3$. Although a few more data points are needed at lower Na/K ratios, varying the ratio does not appear to hold much promise for enhancing carbonation.

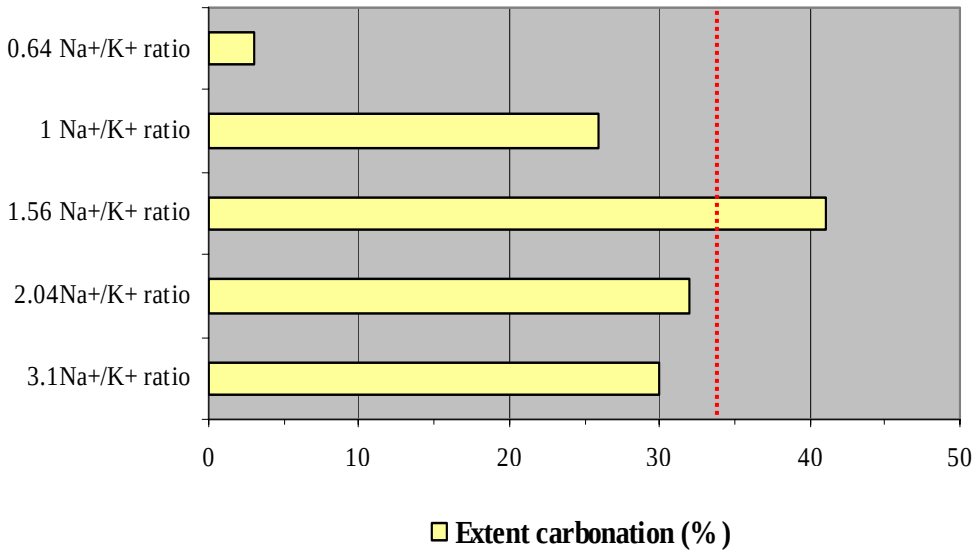

***Figure 3**: Extent of carbonation of San Carlos olivine as a function of Na^+/K^+ molar ratio, at 0.64M HCO_3^-, 1.0M Cl^-, and 1.64M M^+ (M = Na + K). The dotted red line indicates the average extent of carbonation observed using the standard 0.64M $NaHCO_3$ + 1.0M NaCl aqueous solution.*

We also explored the effect of reaction temperature and pressure on the extent of carbonation observed for high bicarbonate concentrations using 2.5 M $NaHCO_3$. $NaHCO_3$ offered the highest extent of carbonation for relatively low, e.g. 2.5M, bicarbonate concentrations (56% vs. 34% for the standard solution 0.64M $NaHCO_3$ + 1.00 M NaCl) and was used as the aqueous solution for these studies. In Figure 5 below, the extent of carbonation of <38µ San Carlos olivine as a function of reaction temperature is shown. The extent of carbonation is clearly very sensitive to reaction temperature, with carbonation decreasing dramatically with decreasing reaction temperature below 185 ^oC. In contrast, a modest increase in the reaction temperature above 185 ^oC did not improve carbonation.

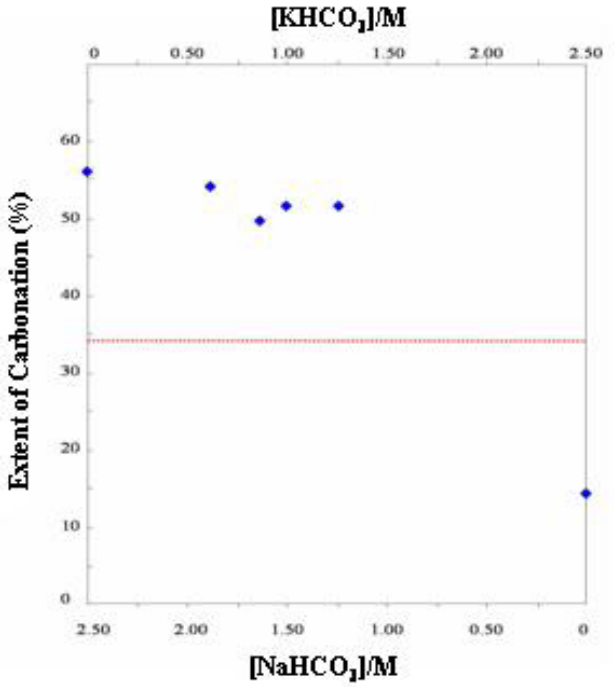

Figure 4: *Extent of carbonation versus the $NaHCO_3/KHCO_3$ ratio. Reaction conditions are: 1h, 185°C, 2200psi CO_2, and stirring at 1500rpm. The $[HCO_3^-]$ was maintained at 2.5M. The dashed horizontal red line represents the extent of carbonation observed using the standard 0.64M $NaHCO_3$ + 1.0M NaCl aqueous solution.*

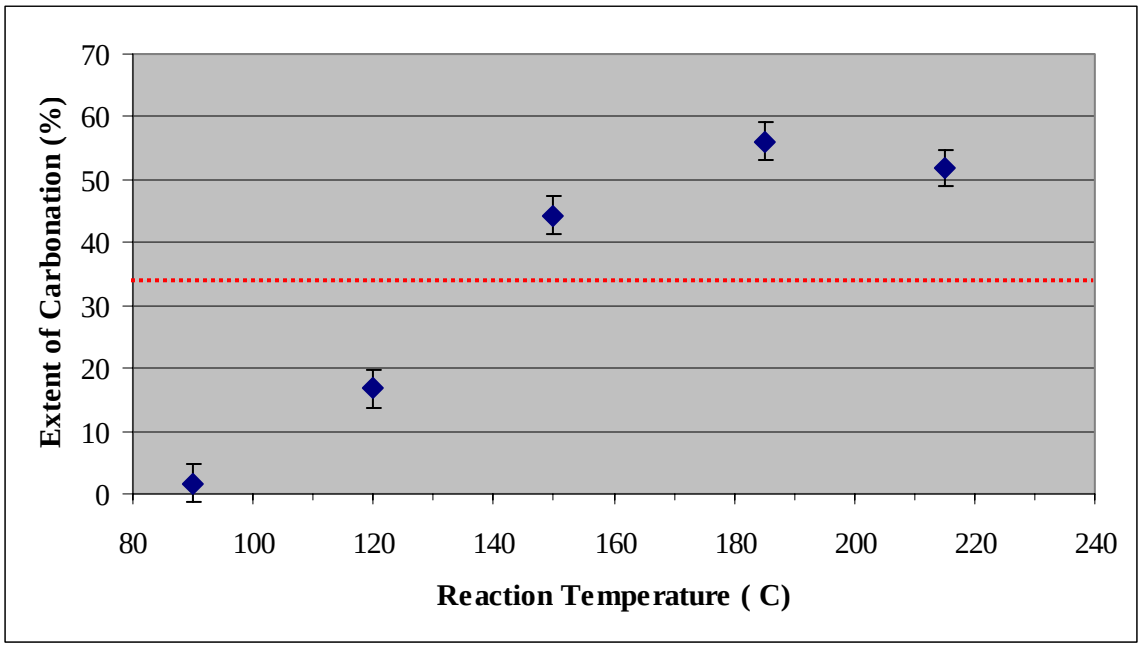

Figure 5 *The effect of reaction temperature on the extent of carbonation of San Carlos olivine (<38µ). Reaction conditions: 1h, 2,200 psi CO_2, 1500rpm stirring, and 2.5M $NaHCO_3$. The dashed red line represents the average extent of carbonation observed using the standard aqueous solution (0.64M $NaHCO_3$ + 1.00 M NaCl) at 185 ^oC.*

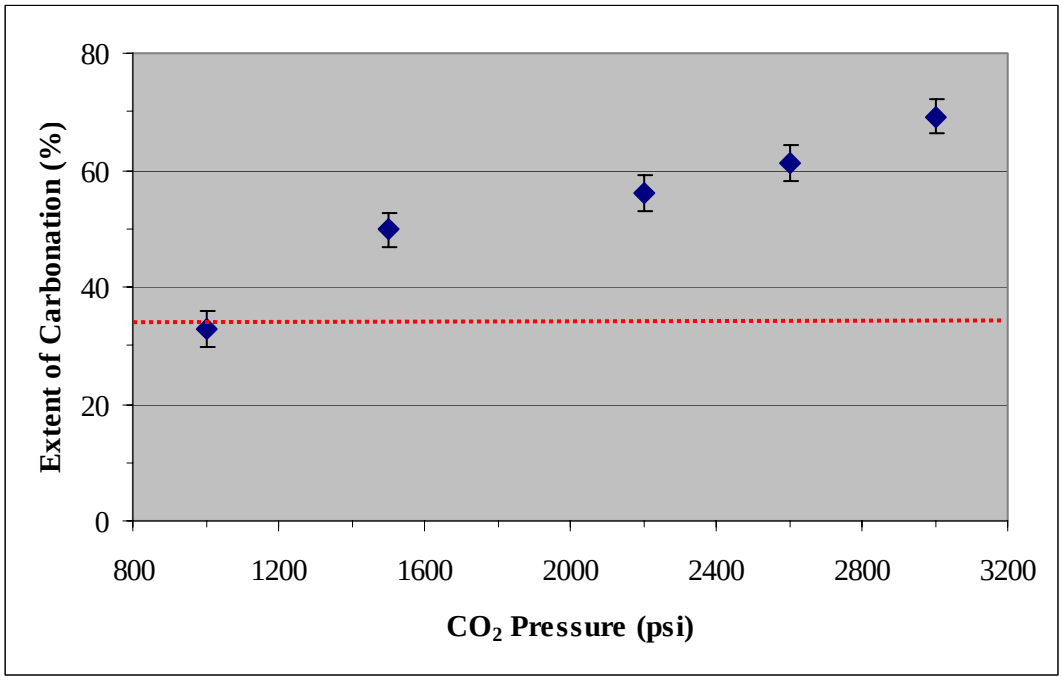

Figure 6: *The effect of reaction pressure on the extent of carbonation of San Carlos olivine (<38μ). Reaction conditions: 1h, 185 °C, 1500rpm stirring, and 2.5M $NaHCO_3$. The dashed red line represents the average extent of carbonation observed using the standard aqueous solution (0.64M $NaHCO_3$ + 1.00 M NaCl) at 2,200 psi.*

Figure 6 shows the effect of reaction pressure on the extent of carbonation observed using 2.5M $NaHCO_3$. 185°C was selected as the optimal carbonation temperature for 2.5M $NaHCO_3$. The same feedstock material (<38μ San Carlos olivine) was tested with the other reaction conditions identical to those used for the reaction temperature studies. The extent of carbonation is a strong function of CO_2 reaction pressure, exhibiting a strong increase in carbonation with increasing pressure (e.g., from 32% at 1,000 psi to 70% at 3,000 psi), consistent with increasing CO_2(aq) activity increasing the extent of carbonation. It is informative to compare these results with our observations for increasing bicarbonate concentrations in Figures 1 and 2. Increasing extents of carbonation with increasing CO_2(aq) activities is further consistent with the hypothesis that increasing bicarbonate concentrations may suppress CO_2(aq) solubility and carbonation for high bicarbonate concentrations. Again, NMR probe and simulation investigations are planned to further explore this possibility by investigating the effect of increasing Na/K bicarbonate concentrations on CO_2(aq) solubility.[11,12]

Scientific Progress: Multi-phase Fluid Modeling and Experimental Investigations to Elucidate Key Slurry-Flow Parameters that Enhance Exfoliation and Carbonation

1. **Exploring the Effect of Feedstock Particle-Size Distribution on Aqueous Olivine Carbonation Reactivity**

Our recent slurry-flow modeling investigations (below) indicate that the spatial olivine particle distribution and the associated velocity vectors during aqueous mineral carbonation (using the

100ml ASU batch reactor) are highly dependent on the feedstock particle size distribution, as discussed below. These studies suggest that controlling the particle size distribution during mineral carbonation may provide a cost-effective avenue to enhance particle abrasion and olivine carbonation. To begin to explore the associated potential to enhance carbonation, the extent of carbonation was explored as a function of the particle-size distribution associated with 10 gram San Carlos olivine mineral carbonation feedstock samples. The extent of carbonation for particle size fractions of freshly ground and wet-sieved San Carlos olivine were investigated in both the standard 0.64M $NaHCO_3$ + 1M NaCl and 2.5M $NaHCO_3$ aqueous solutions. Duplicate runs using the standard solution gave reproducible extent of carbonation results for these feedstock batches as follows: <38μ feedstock: 37%; 38-75μ feedstock: 5%; 75-150μ feedstock: 4%.

The <38μ and 38-75μ batches were mixed to generate <75μ fractions with different weights of the <38μ and 38-75μ particle size fractions. The extent of carbonation observed using the standard aqueous solution (0.64M $NaHCO_3$ + 1M NaCl) for the various particle size distributions is shown in Figure 7. The average extent of carbonation observed above for the <38μ and 38-75μ particle-size fractions were used to calculate the "predicted" extent of carbonation if carbonation is independent of the feedstock particle size distribution. The predicted extents of carbonation are compared with the experimental results for a series of mixtures of the <38μ and 38-75μ particle size fractions in Figure 7. In this case, varying the particle size distribution by blending different amounts of the 38-75μ fraction with the <38μ fraction did not significantly impact the extent of carbonation observed, indicating in this case varying the particle size distribution did not significantly impact particle abrasion and exfoliation. In other words, the <38μ and 38 to 75μ feedstock materials appear to experience the same extent of carbonation independent of the wt% ratio used.

The extent of carbonation was also explored for select <38μ, <75μ, and <150μ feedstock materials using an aqueous 2.5M $NaHCO_3$ solution to probe whether the highly reactive aqueous solution chemistry associated with high bicarbonate concentrations impacts the relative reactivity of different particle size distributions. In this case, we explored the relative carbonation reactivity of the above particle size ranges for the standard 0.64M $NaHCO_3$ + 1M NaCl and 2.5M $NaHCO_3$ aqueous solutions. Figure 8 compares the average extent of carbonation observed for the above particle-size fractions for both solutions. A 35% improvement in carbonation is observed for the <38μ fraction using 2.5M $NaHCO_3$. By comparison, a 146% and 158% improvement is observed for the <75μ, and <150μ fractions, respectively, suggesting high concentration bicarbonate solutions can substantially further enhance the relative carbonation reactivity of larger olivine particle-size fractions. Being able to effectively carbonate olivine feedstocks with such larger particle-size fractions offers the potential to substantially reduce feedstock grinding cost and substantially lower mineral sequestration process cost.

2. Exploring the Effect of Abrasive Slurry Additives on Passivating-Layer Exfoliation and Olivine Carbonation

To further explore the role of particle abrasion on the extent of carbonation, quartz particles were

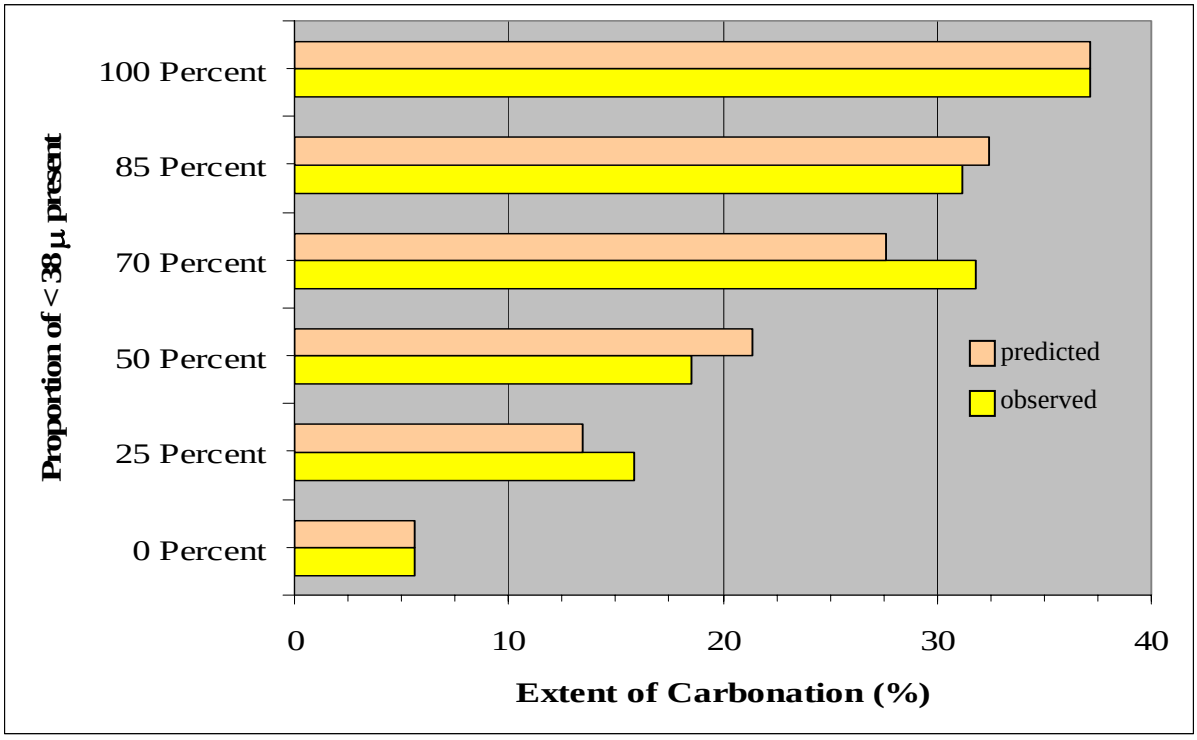

Figure 7: *Effect of mixing <38µ and 38-75µ fractions on the extent of carbonation of San Carlos olivine using the standard aqueous 0.64M $NaHCO_3$ + 1M NaCl solution, with a reaction time of 1h at 185 ^oC, under 2200psi CO_2, and with ~1500rpm stirring. The proportion of <38 µ olivine used is given in weight percent.*

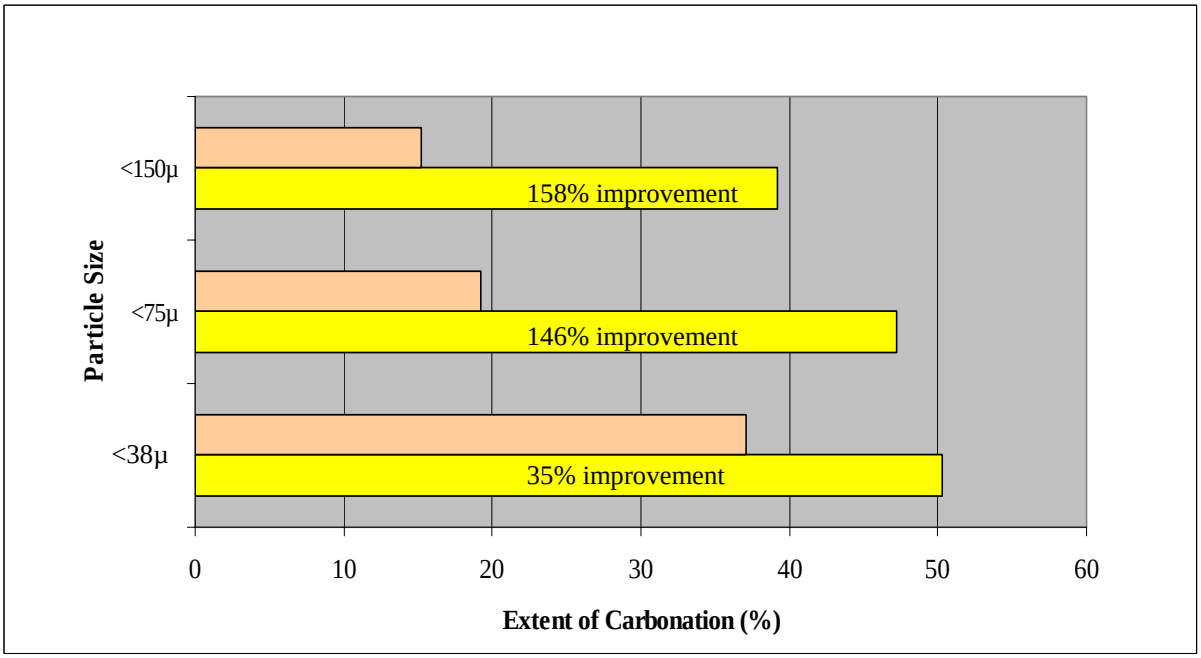

Figure 8: *Effect of particle size distribution on the extent of carbonation observed for San Carlos olivine using the standard (0.64M $NaHCO_3$ + 1M NaCl) aqueous solution (orange bars) and 2.5M $NaHCO_3$ aqueous solution (yellow bars). Note the dramatic improvement in the extent of carbonation observed for the larger particle-size feedstock material when 2.5M $NaHCO_3$ is used.*

incorporated during olivine mineral carbonation as a potential abrasive agent for promoting passivating-layer exfoliation and carbonation. In this case, synthetic olivine (forsterite: Mg_2SiO_4) was used as the feedstock. The weight % quartz was varied from 0 to 80% of the 10g feedstock charge used. The carbonation studies were performed using the standard aqueous solution (0.64M $NaHCO_3$ + 1M NaCl), with the reactions carried out for 1h at 185°C under 2200 psi CO_2, with ~1500rpm stirring. The results are shown in Figure 9. Without the addition of the quartz abrasive, a 68% extent of carbonation was observed. The extent of olivine carbonation observed increased with increasing wt. % quartz up to 84% carbonation for 60 weight % quartz, consistent with enhanced passivating-layer abrasion. However, carbonation decreased at higher quartz concentrations (i.e., 80 wt. %), which may be associated with increasing quartz-quartz particle abrasion reducing its effectiveness at passivating-layer abrasion. To explore this hypothesis, 10g of quartz was run for an hour under the same mineral carbonation conditions, including 1,500 rpm stirring to simulate the enhanced quartz-quartz abrasion that may occur when high quartz concentrations are used as an abrasive to enhance olivine carbonation. The product was filtered, rinsed, and dried. 6g of the "abraded quartz" was run with 4g of forsterite to explore its abrasive potential. As seen in Figure 9, the extent of carbonation is substantially lower than that observed with fresh quartz, consistent with self abrasion reducing the effectiveness of quartz as a passivating-layer abrasive agent at higher quartz concentrations. This reduced effectiveness may be associated with both particle-size reduction and smoothing of the quartz particle edges at higher quartz concentrations.

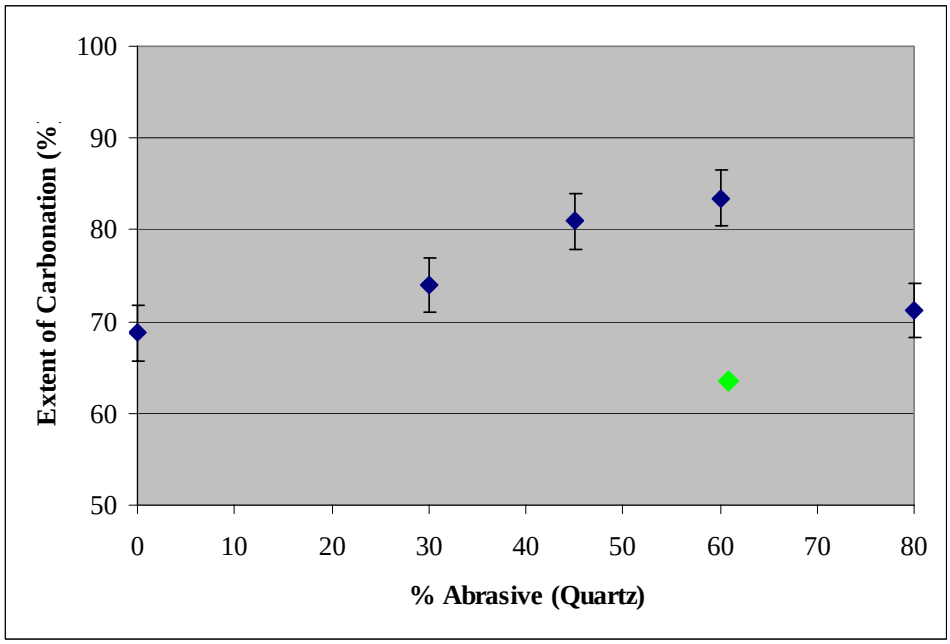

Figure 9: *Extent of carbonation observed for synthetic olivine as a function of the wt. % quartz abrasive added (blue diamonds). Reaction conditions are 0.64M $NaHCO_3$ + 1M NaCl, 1h, 185°C, 2200 psi CO_2, and 1500rpm stirring. The green diamond shows the extent of carbonation observed using self-abraded quartz particles.*

3. Effect of Quartz Abrasives on Carbonation as a Function of Temperature

As reaction temperature may affect the properties of the passivating layers that form during

olivine carbonation, we explored the impact of temperature on the effectiveness of quartz passivating-layer abrasion. Two preliminary runs were conducted with 10 and 20 wt% quartz. 10 wt% did not significantly enhance carbonation, whereas 20% was effective. Figure 10 shows the extent of olivine carbonation with and without the addition of 20 wt% quartz abrasive. Significant enhancement in the extent of carbonation is observed over the range of temperatures where carbonation is reasonably effective, indicating that abrasive quartz additives are effective at enhancing passivating-layer exfoliation and carbonation at least from 155 to 215 ^{o}C. It is particularly interesting to note the extent of carbonation observed with and without the quartz abrasive at 185 ^{o}C. In this case, the enhanced extent of carbonation observed is greater per 10g of feedstock (61% vs. 56% per 10g feedstock), even though 20% of the feedstock, quartz, cannot carbonate. This key observation indicates that controlled use of low cost abrasives may offer the potential to reduce mineral sequestration process cost. Any effort to optimize carbonation with such controlled abrasive additions should, of course, be integrated together with control of the slurry fluid-flow conditions to maximize particle abrasion and passivating-layer exfoliation.

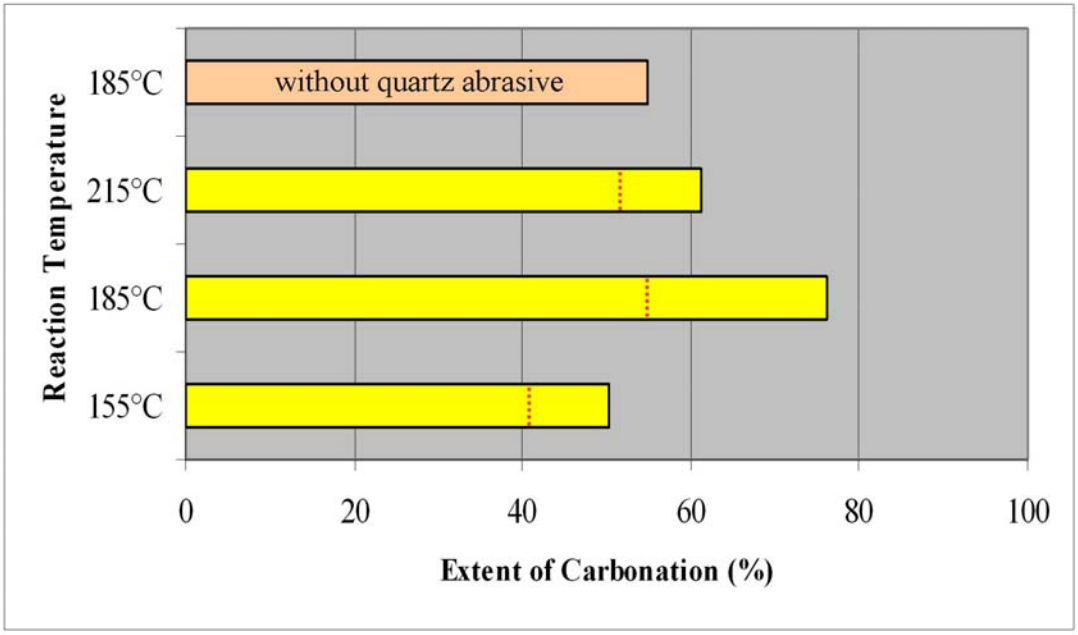

Figure 10: *Extent of carbonation of <38μ San Carlos olivine, mixed with 20 wt% quartz abrasive as a function of reaction temperature. The carbonation conditions are 1h reaction time, 2200psi of CO_2, and 1500rpm stirring using a 2.5M aqueous $NaHCO_3$ solution. The full yellow bars indicate the extent of carbonation with the quartz abrasive. The dashed vertical red lines indicate the extent of olivine carbonation observed in the absence of the quartz abrasive for the same olivine feedstock batch.*

4. Effect of Quartz Abrasives on Carbonation as a Function of Reaction Pressure

Since the reaction pressure may affect the properties of the passivating layers that form during olivine carbonation, we also explored the impact of pressure on the effectiveness of quartz passivating-layer abrasion. The optimal reaction temperature in Figure 10 (185 ^{o}C) was selected for these investigations, with 20 wt% quartz again used as the passivating-layer abrasive. The

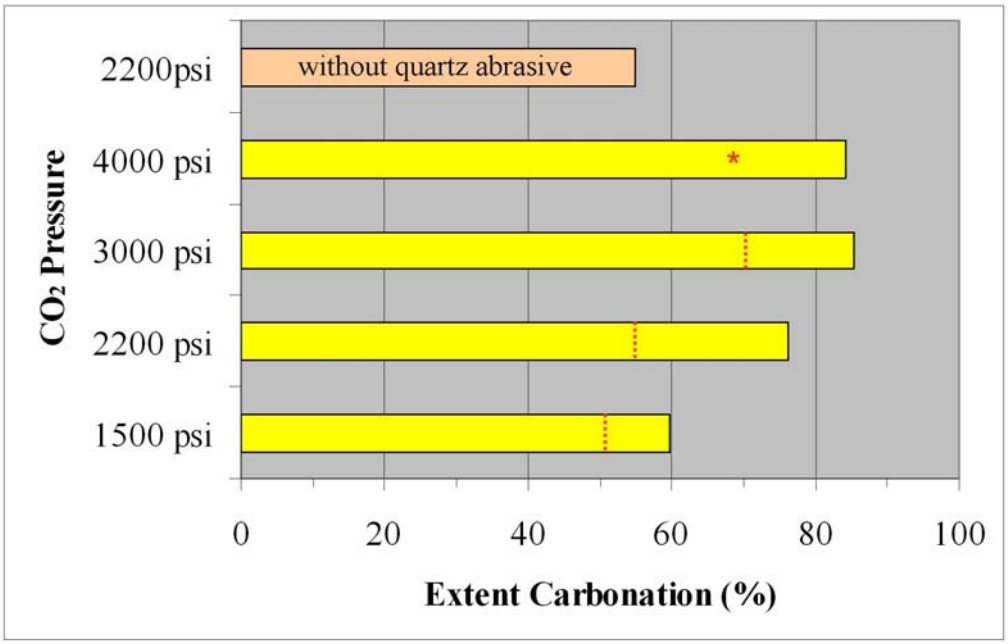

Figure 11: *Extent of carbonation of <38μ San Carlos olivine, mixed with 20 wt% quartz abrasive as a function of reaction pressure. The carbonation conditions are 1h reaction time, 185 ^{o}C, and 1500rpm stirring using a 2.5M aqueous $NaHCO_3$ solution. The full yellow bars indicate the extent of carbonation with the quartz abrasive. The dashed vertical red lines indicate the extent of olivine carbonation observed in the absence of the quartz abrasive. The extent of carbonation at 4,000 psi in the absence of the quartz abrasive* has not yet been explored.*

quartz abrasive was observed to effectively enhance olivine carbonation over the range of pressures studied to date (1,500 to 3,000 psi), as shown in Figure 11, indicating that quartz is effective as a passivating layer abrasive over a range of pressures as well as a range of temperatures. The above studies as a function of pressure and temperature indicate the silica-rich passivating layers that form retain their brittleness and ability to exfoliate over a range of reaction temperatures and pressures relevant to aqueous olivine mineral carbonation.

The above observations underscore the importance of passivating-layer exfoliation/abrasion in enhancing olivine carbonation reactivity. In these studies, quartz was selected as a model low-cost abrasive that should not significantly impact the aqueous solution chemistry, hence providing insight into the potential abrasives offer to enhance carbonation. The addition of such abrasives is not limited to quartz or the slurry-flow conditions described herein. Indeed, these results suggest that a reaction process that offers the potential to better enhance feedstock abrasion, such as a fluidized-bed approach, may lead to significant further improvements in carbonation reactivity. In either case the associated slurry/fluidized bed flow dynamics can greatly impact the effectiveness of passivating layer abrasion/exfoliation and olivine mineral carbonation reactivity.

5. Exploring the Slurry-Flow Dynamics during Olivine Carbonation via Multiphase Fluid Modeling

During the first project year, work in this area of the project focused on two hierarchies of multiphase fluid-flow modeling. Both microscopic and macroscopic approaches were applied. The over-arching aim of the investigations in this portion of the project is to attempt to isolate and to understand effects that may be crucial to optimizing the fluid dynamics of sequestration processes to enhance passivating layer exfoliation and carbonation. The simulations used to assess "microscopic" fluid flow modeling illustrated that particle transport and mixing can be enhanced by interactions with roughened surfaces. While the current simulations used to assess the roughness model are idealized, in order to enable the application of simulation techniques that resolve turbulent fluctuations, the computations illustrated the importance of the basic effect of roughness, which is to transfer the mean streamwise momentum of the particles to the fluctuating velocities that are normal to the surface. This is an important mechanism for enhancing transport across the entire channel and facilitating particle-particle and particle-wall collisions, exfoliation and carbonation.

Macroscopic approaches, which emphasized simulating the slurry-flow behavior of a section of the Albany Research Center's (ARC's) flow-loop reactor,[8] indicated that the reactant particle size distribution may be a key factor that affects particle collision frequency, momentum transfer, exfoliation and carbonation. Due to the complexity of the flow-loop reactor, we have emphasized full system simulations of the 100ml batch ASU minireactor during the second year of this project. Such simulations have the decided advantage that they can provide insight into whole system slurry-flow dynamics, which can be directly compared with experiment. Once the impact of the slurry flow dynamics are better understood in the ASU batch reactor, the developed understanding can then be transferred to develop a better understanding of the effects that the slurry-flow dynamics have on olivine mineral carbonation in the ARC flow-loop reactor shown in Figure 12.

Figure 12: *The Albany Research Center's Flow-Loop Reactor.*

The primary focus of the slurry-flow modeling investigations during the second project year has been on developing a better understanding of the impact that the slurry-flow dynamics can have on olivine carbonation and passivating layer exfoliation at the macroscopic level for reactions carried out using the 100 ml ASU minireactor. The multiphase slurry in the minireactor is being modeled using Computational Fluid Dynamics (CFD) via Fluent. An example of the motivation for the simulations of the slurry dynamics in the minireactor comes from the wide variation in extent of carbonation observed for the same feedstock materials, such as the 23% vs. 2% extent of carbonation observed for <150μ Twin Sisters olivine run in the ASU minireactor and ARC flow-loop reactor, respectively. Experimental measurements of the extent of carbonation as a function of solids size fraction -- expressed in terms of the surface area available for reaction -- are summarized in Figure 13. As seen in the plot, the decrease in the surface area available for carbonation results in a decrease of the extent of carbonation, however, the decrease is not reflected to the same degree for both reactors, with the flow-loop reactor exhibiting anomalously low carbonation for the <150μ Twin Sisters olivine. This poor correlation becomes particularly interesting as different methods are employed to agitate the slurry in each of the reactors, underscoring that the slurry-flow dynamics incorporated during carbonation can dramatically impact the extent of carbonation observed. As discussed above, our second year slurry-flow modeling investigations have focused on whole system simulations of the ASU minireactor.

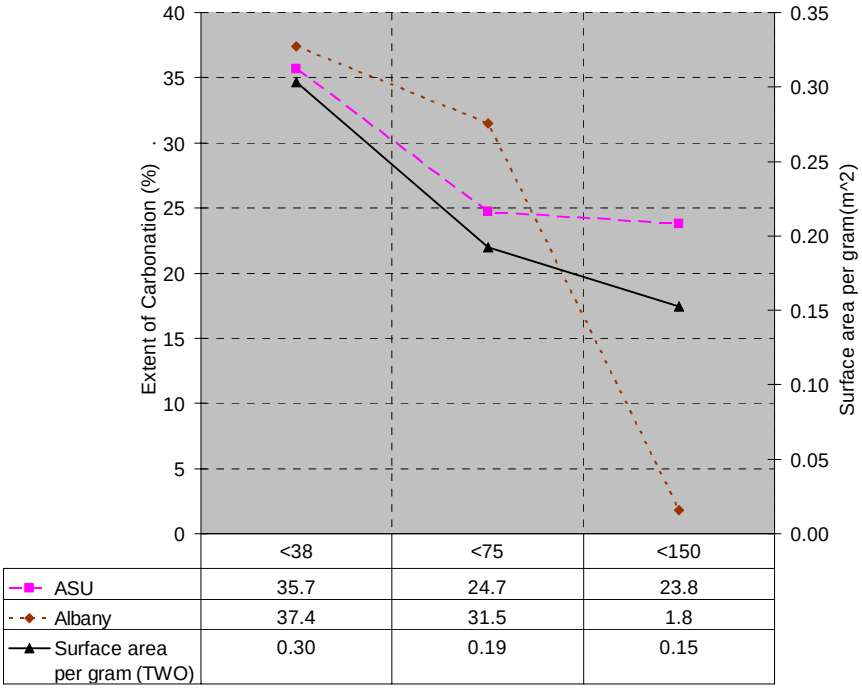

Figure 13: *Surface area available vs. extent of carbonation measured for the <150μ Twin Sisters Olivine (TWO) samples using the 100ml ASU batch minireactor and the ARC flow-loop reactor.*

Herein, we summarize the overall methodology of the simulations, consisting of generation of a three-dimensional grid representing the reactor geometry, computing the flow properties via solution of the model equations developed to describe the system, and analysis of the results. The computations are performed using the commercial software Fluent, which includes the

module Gambit used to generate the grids. Post-processing and analysis are also accomplished using Fluent.

Simulation Overview

Grid generation is the process of subdividing a region of interest into a set of small control volumes, which are then used to resolve the equations used to model the slurry. Associated with each control volume are one or more values of the dependent flow variables, which in this work are the phase velocities, pressure, volume fraction, turbulent kinetic energy, and dissipation rate. The model equations corresponding to the equations for conservation of mass, and momentum are solved numerically using the finite-volume method available in Fluent.

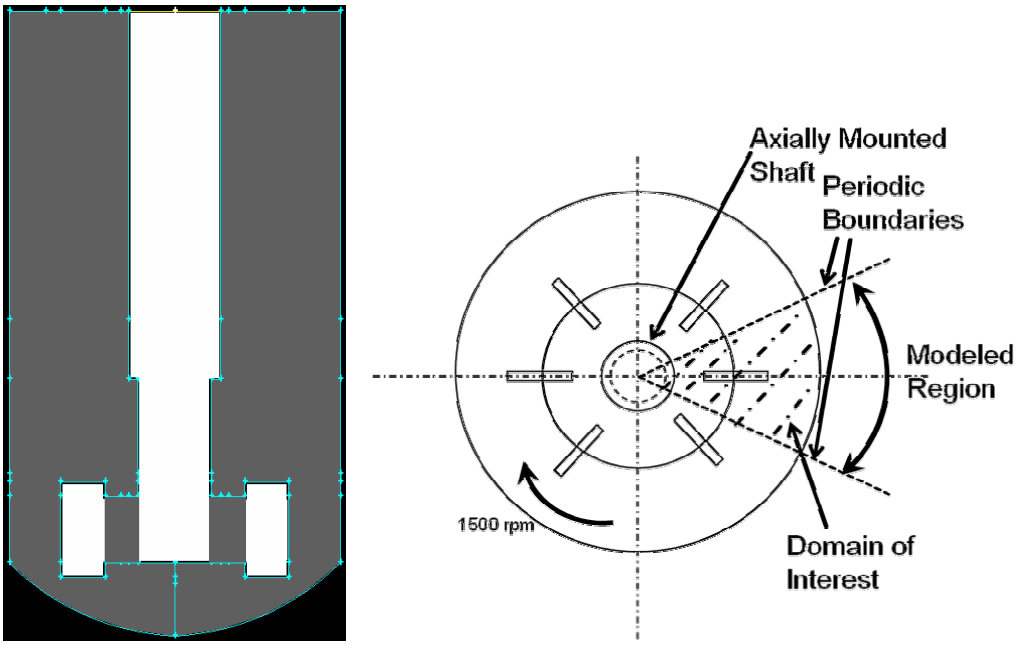

Figure 14: *(a) Wireframe view of the ASU mini-reactor, gray portion indicating the flow region and white portion indicating the rotating shaft and paddles; (b) Top view of the reactor highlighting the paddles, the central shaft, and the periodic boundaries applied to the computational domain (Figure not to scale).*

The ASU minireactor geometry is modeled using Gambit in which a computational mesh is created within a computer-aided drawing of the reactor vessel. Figure 14(a) shows a wireframe view of the minireactor. The minireactor used at ASU consists of a hollow cylindrical container with a nearly hemi-spherical bottom. A shaft attached to a motor runs centrally along the axis of the cylinder. A set of six blades arranged at 60 degree increments are attached to the shaft, which rotates at 1500 rpm. This top view is depicted in Figure 14(b). A spiral cooling tube is entwined around the central shaft, through which cold water is circulated during the post-reaction cooling process. A metal lid closes the top of the reactor during the carbonation process which is carried out for one hour in the experiments. To simplify mesh generation and reduce the simulation time, the spiral tube that transports cooling water during the post-reaction step

was not included in the computational representation of the minireactor. To reduce the computational expense, symmetry conditions were utilized to advantage with a grid generated for 1/6th of the reactor. Periodic conditions as shown in Figure 14(b) were applied to the solution variables at the bounding planes. Periodic boundary conditions ensure that the volume of fluid and particles crossing either of the bounding planes migrate back into the domain at the other plane.

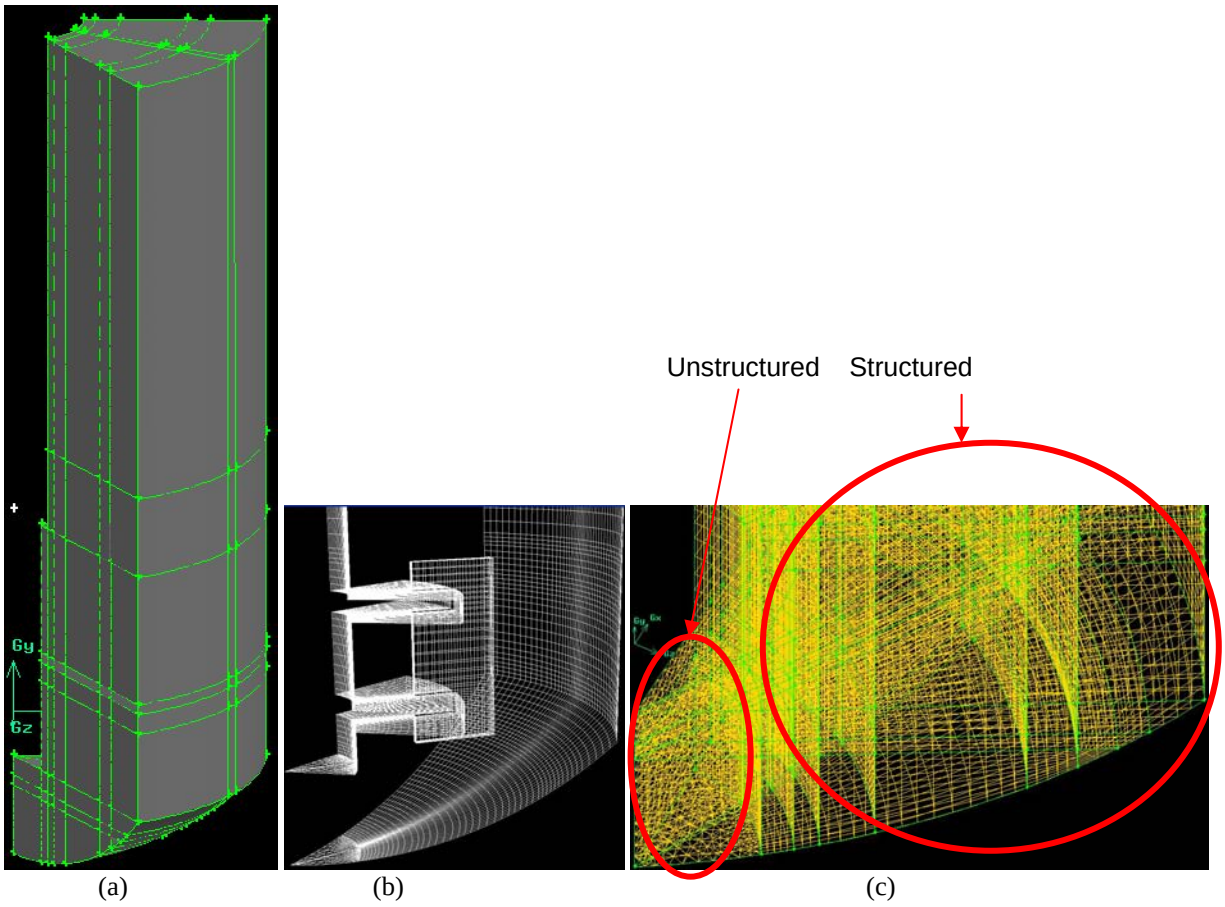

Figure 15: *Isometric views of (a) the solid section modeled (b) open view of the paddle wheel with the periodic faces removed (c) zoomed view of the lower region with the unstructured mesh.*

The steps comprising the mesh generation process are creation of nodes/vertices that define the geometry, joining the nodes to form edges, joining the edges to form surfaces and in the present simulations, due to the cylindrical shape of the reactor, by revolving the surfaces to form volumes. Following this process, meshing of the volume was accomplished by first generating a grid along the edges, followed with the faces and finally by extending the meshing process to accommodate the volumes. To simplify the grid generation process, the entire reactor was divided into smaller zones, which were then meshed individually. The mesh generated for the minireactor consisted of both structured and unstructured mesh elements. The bottom region of the cylinder could be meshed using either structured or unstructured grid elements. However, meshing the lowermost part of the container using a structured grid resulted in distortion of the geometry and an inaccurate representation of the hemi-spherical bottom. To avoid a drastic

change in the geometry of the model, an unstructured grid was used, which helped retain the near hemi-spherical shape of the bottom of the cylinder. Figure 15(a) shows the solid view of the modeled section. Figure 15(b) shows the open view of the paddle wheel with the mesh on the faces of the blades and the wall, while Figure 15(c) zooms in on the unstructured part of the geometry. The initial mesh that was generated consisted of approximately 2.25 million cells. The grid generation task was repeated in order to develop a coarser grid consisting of approximately 140,000 cells that enables relatively efficient simulations to be performed.

Mathematical Model

The mathematical model is based on an Eulerian-Eulerian approach in which the secondary phase (olivine) is treated as a continuum. The commercial flow solver Fluent was used to solve the mass conservation equation (Equation 1) and momentum equation (Equation 2) for each phase.

$$\frac{\partial}{\partial t}\left(\alpha_l \rho_l\right) + \nabla \cdot \left(\alpha_l \rho_l \vec{v}_l\right) = 0 \tag{1}$$

$$\frac{\partial}{\partial t}\left(\alpha_l \rho_l \vec{v}_l\right) + \nabla \cdot \left(\alpha_l \rho_l \vec{v}_l \vec{v}_l\right) = -\alpha_l \nabla p + \nabla \cdot \bar{\bar{\tau}}_l + \alpha_l \rho_l \vec{g} + \sum_{l=1}^{n}\left(K_{ls}\left(\vec{v}_l - \vec{v}_s\right)\right) \tag{2}$$

Here α_l represents the volume fraction of phase *l* (liquid phase), while the density is represented by ρ. $\vec{v}_l$ and $\vec{v}_s$ represent the velocity of liquid phase *l* and solids phase *s*, and the pressure which is uniform across all the phases is represented by *p*. $\bar{\bar{\tau}}_q$ represents the solids stress tensor, *g* represents the acceleration of gravity and K_{ls} accounts for the momentum transfer between the solids and liquids phase. The momentum equation governing the solid phase is analogous to the momentum equation for the liquid phase, wherein each term representing the liquid phase (*l*) is replaced with a corresponding solid phase term (*s*).

To obtain a solution of the momentum equations, the *k-ε* model was used.[13] Since the volume fraction of olivine used in the reactor is high, a discrete phase solution approach is employed in which separate equations are defined for each phase. In the present effort, the primary phase consists of an aqueous solution-CO_2 mixture and with olivine particles comprising the secondary phase. External forces such as virtual mass (which occurs when the particulate phase accelerates relative to the fluid phase) and lift forces (acting on particulate phase mainly due to velocity gradients in primary phase flow field) are neglected in the computations that have been performed to date. Solving equations 1 and 2 require several constitutive relationships. For example, a model proposed by Gidaspow[14-16] to model the interphase momentum transfer term is employed and takes the form,

$$K_{sl} = \frac{3}{4} C_D \frac{\alpha_s \alpha_l \left|\vec{v}_s - \vec{v}_l\right|}{d_s} \alpha_l^{-2.65},$$

where C_D represents the coefficient of drag and is related to the Reynolds number (Re_s) as:

$$C_D = \frac{24}{\alpha_l \,\mathrm{Re}_s}\left[1 + 0.15\left(\alpha_l \,\mathrm{Re}_s\right)^{0.687}\right].$$

An important term governing the motion of the particulates is the fluid-particle interaction force, which is expressed as a function of the relative velocity between the solids and the aqueous phase $\left|\vec{v}_s - \vec{v}_l\right|$.

Solution Procedure and Results

Following the grid generation step, the grid was imported into Fluent where flow properties were defined that model the aqueous solution-carbon dioxide mixture and olivine ore in the closed cylinder. To solve the partial differential equations summarized above, approximate initial and boundary conditions are needed for realistic simulations. The boundary values along the walls were set to represent a no-slip boundary condition and the boundary value for the impeller blades were set to represent an angular velocity corresponding to a shaft speed of 1500 rpm. Initially, the simulations were carried out for cases corresponding to steady state in the reactor (a representation corresponding to a long-time average of the state of the minireactor). Solution of the steady-state flow enables a computationally efficient view of the system. To obtain a steady-state solution, the simulation process for obtaining the flow solution was divided into two stages, the first stage was the solution of the flow for the aqueous phase/CO_2 fluid mixture (only), the converged solution of which forms the initial condition for the second stage in which the solids phase was incorporated. Ten grams of olivine, as used in the ASU experiments, was added to the bottom of the cylinder. The height to which the olivine settles when filled in the reactor was measured experimentally and this height was patched as the initial distribution of olivine in the model. In the simulations, the solids phase was initially prescribed at the bottom of the reactor vessel at the maximum permissible packing limit of 63%.

The NIST Chemistry web-book (http://webbook.nist.gov/chemistry/fluid/) was used as a reference to obtain values for density and viscosity of water and CO_2 for use in the simulations. Density values for the water-CO_2 mixture were obtained by taking an average of the densities of water and CO_2. Since the viscosity calculations do not follow the average rule, and since there are no known experimental values of viscosity of the aqueous mixture (of water and CO_2) under the specified temperature and pressure, the current simulations were performed using the viscosity of water at the elevated conditions (150 atm and 185^{o}C) as the viscosity of the aqueous phase/CO_2 fluid mixture. The simulations do not account for temperature variations in the mixture, i.e., an isothermal system is computed with the elevated temperature being reflected in the density and viscosity values of the mixture. Coupling between the fluid and solid phases is achieved using inter-phase momentum transfer terms that account for the momentum transfer between the granular olivine phase and the mixed-fluid phase formed by mixing water and CO_2. The paddle blades along with the central shaft rotate at 1500 rpm. This is accounted for in the simulations by sliding parts of the mesh around the blades through the remainder of the grid.

Initial simulations were performed using a time step of 1 second. Considering the rotational speed of the impeller in the reactor at 1500 rpm, a time step of 1 second corresponds to 25 revolutions or 9000 degrees. These initial studies were performed using this relatively large time

step in order to provide a preliminary assessment of the influence of particle size on the subsequent flow field solutions. The results obtained indicate that substantial differences exist in the phase distribution and velocity distribution patterns for different particle size fractions.

Following these initial computations, the simulations for the unsteady phase were performed using much smaller time steps in order to improve the temporal accuracy of the CFD model. The time-step used in the unsteady simulations correspond to a paddle wheel rotation of approximately 5 degrees per step. Numerical tests show that convergence of the system of equations occurs after approximately 25 iterations within each time step. Preliminary simulations performed with smaller time-steps (2 degrees per time step) did not yield significant changes in the results, justifying the time step corresponding to 5 degrees of revolution.

The simulations have been performed for two size fractions: a solids phase consisting of 37μ diameter particles and a second simulation using 150μm diameter particles. Simulations for a size fraction of 75μ diameter particles are being performed during the current no-cost extension period (the number of concurrent calculations is limited by a fixed number of licenses, we have invested in 4 additional licenses during the no-cost extension to enhance system evaluation.)

Steady state as well as time accurate solutions representing the flow field in the minireactor were obtained using first-order accurate discretization of the model equations. Using current resources, the time required to compute 1000 iterations of the multiphase solution is approximately 24 hours on a single processor AMD Athlon 64 bit 2.0GHz workstation equipped with 2 GB memory. Each iteration computes the values of flow variables in every cell of the domain. This process is continued until the difference in the values of the flow variables (residuals) between consecutive iterations is O(1e-6).

Figures 16(a) and 16(b) show the aqueous-phase velocity vectors in the steady-state solution for the single phase (aqueous mixture of water and CO_2 only) case. While Figure 16(a) shows the velocity vectors colored by the absolute velocity, Figure 16(b) shows the velocity vectors colored by the radial velocity. The figures show that the fluid velocities are largest in the vicinity of the paddle, as expected, given the entrainment and mixing produced by the paddle. In addition, a closer inspection of the figures shows that the vectors in different axial planes away from the paddle possess different orientations, indicative of mixing effects even at relatively larger distances from the paddle.

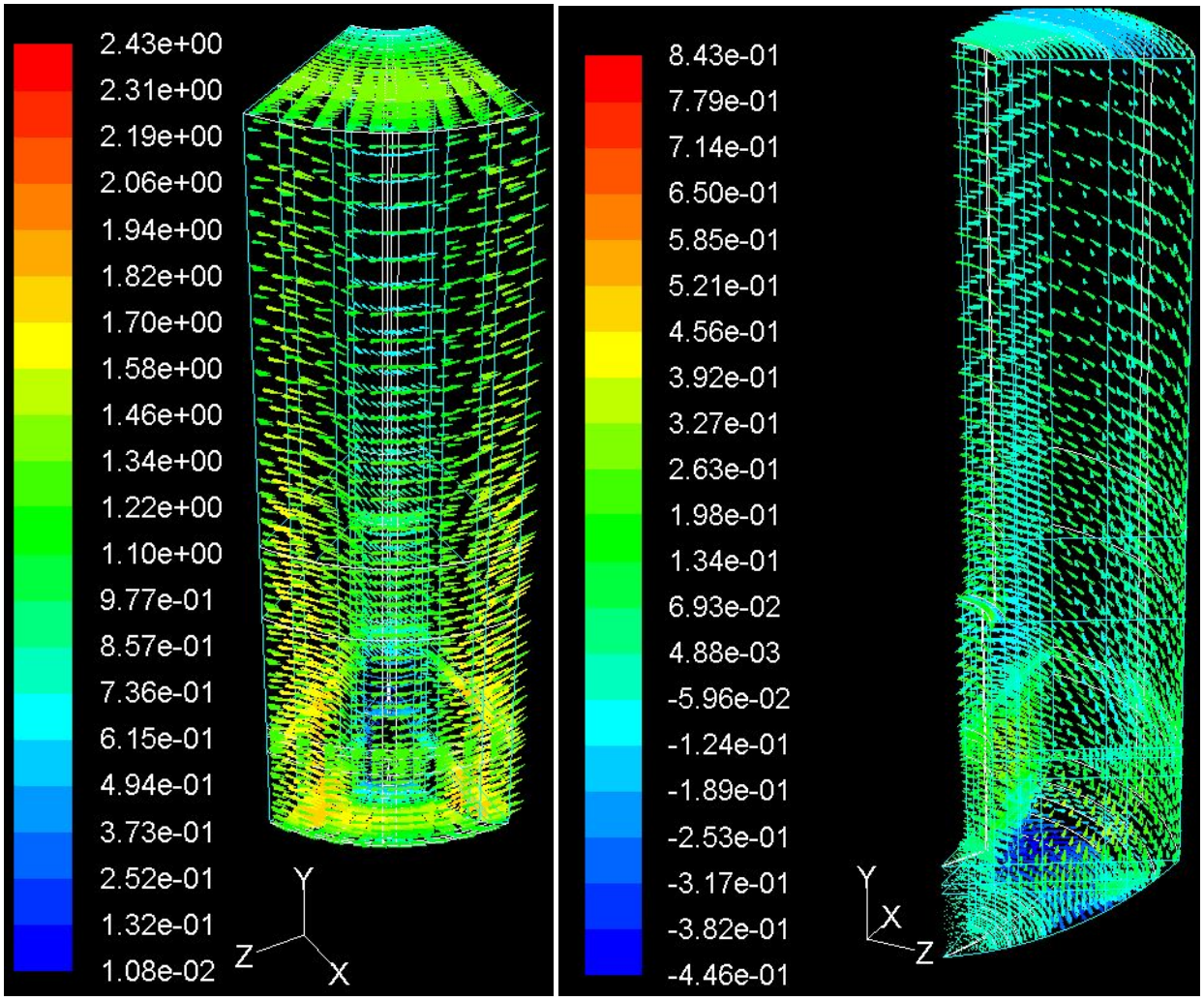

(a) (b)

Figure 16: *Aqueous-phase velocity vectors for the single phase flow, (a) shows the vectors colored by absolute velocity, (b) shows the vectors colored by radial velocity. The vectors indicated in (a) and (b) point counter-clockwise indicating the rotation existing in the cylinder due to the presence of the moving paddlewheel (units in m/s).*

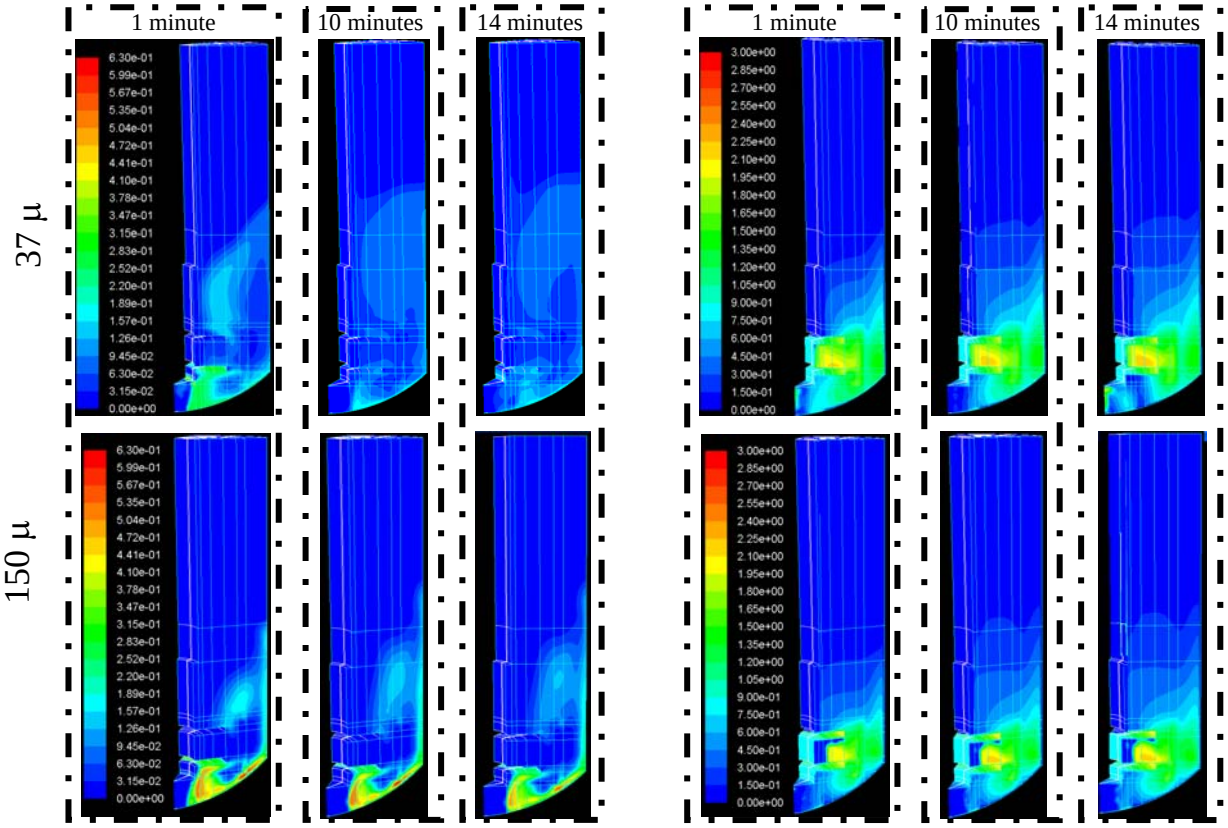

Figure 17: *Contours of (a) volume fraction of olivine, values in fraction, shown to the left (b) velocity distribution of olivine, using larger time step value (dt = 1 second), values in m/s, shown to the right.*

Figure 17 shows contours of the olivine volume fraction distribution for the 37μ case and the 150μ case for time intervals corresponding to t=1, 10 and 14 minutes from the start of the paddle-wheel rotation. A clear demarcation can be observed in the contours, red indicating higher values and blue indicating lowering values of volume fraction. The figure shows that the olivine volume fraction for the 150μ runs exhibits a substantially higher concentration at the bottom of the cylinder and that the contours for the 37μ run correspond to smaller gradients indicative of a substantially greater mixing of the particles with the fluid mixture. This is expected because lighter particles with lower inertia are more susceptible to follow the fluid flow patterns. Larger particles on the other hand behave in a manner that is consistent with their higher inertia. Figure 17(b) shows contours of the particle velocity distribution for the corresponding cases for the same time intervals. Higher velocity is observed near the vicinity of the paddle wheel due to the rotation. The contour profiles indicate the swirling movement of the olivine particles, which are shown to gradually rise toward the top of the reactor, from their initial location at the reactor bottom.

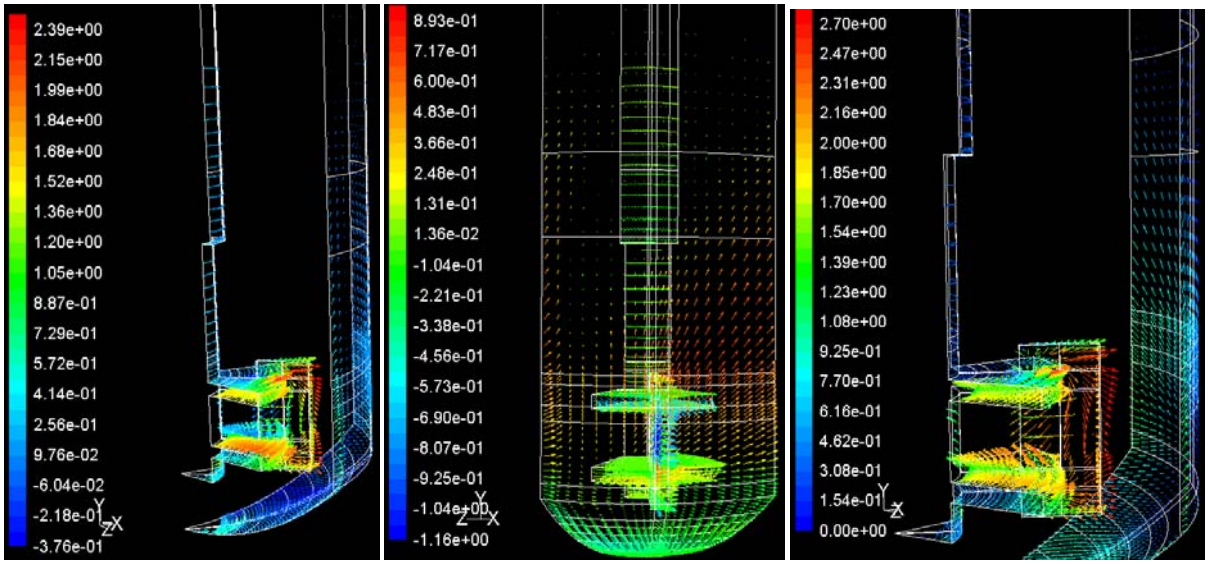

(a) (b) (c)

Figure 18: *Contours of velocity of olivine after t=2 seconds in the reactor colored by (a) x-velocity component, (b) y-velocity component, (c) relative velocity magnitude, values in m/s. (37μm case and time step of 5.56e-4 seconds)*

Phase distribution patterns for the large time step case indicate that substantial differences do exist for the particle behavior of each size fraction. To obtain more accurate results, the time step for each calculation was reduced from 1 second (corresponding to 9000 degrees of revolution) to dt=5.56e-4 seconds (corresponding to 5 degrees of revolution). Figure 18 displays the velocity vectors of olivine within the reactor for simulations corresponding to a time step of 5.56e-4 seconds. The magnitude of the individual velocity components are observed to be as high as 2.39 m/s within the reactor, as seen in Figure 18a. Rough estimates indicate that two olivine particles approximately 15μm in diameter colliding each other at 1 m/s can cause a fracture. Velocity vectors indicate that the paddle wheel causes the olivine particles to accelerate to speeds of up to approximately 2.4 m/s. Olivine particles impinging on each other and with the reactor walls or paddle blades with those high velocities are highly susceptible to fracture. This can be contribute as one of the possible mechanisms that cause a reduction in particle size during carbonation within the reactor. Also, velocity vectors in Figure 18(a) indicate a negative velocity at the hemi-spherical bottom of the reactor, while positive velocities are found in regions at the center of the paddle wheel. This velocity pattern indicates entrainment of the particles towards the center in region below the paddle wheel, while the particles are thrown towards the wall in the region near the paddle wheel center. Similarly, velocity vectors indicate that particles are entrained towards the central shaft in the region above the paddle wheel. This indicates two swirling motions, one counter-clockwise and one clockwise in regions above and below the paddle wheel respectively. Figure 18b shows the y-velocity component of the olivine particles. At the wall of the reactor vessel, the velocity vectors are directed upwards, which indicates olivine particles being pushed to the top section of the reactor. Furthermore, in the zone near the axially located shaft, the y-velocity vectors are negative, which indicate the swirling motion of the particles from bottom to the top at the wall and from the top to the bottom at the axially mounted shaft. However, the results shown above indicate the distribution at t=2

seconds and these simulations need to progress further in time to determine the time dependence on the distribution of olivine particles. Figure 18c shows the relative velocity of olivine within the reactor. The relative velocity is observed to be as high as 2.7 m/s and, as mentioned before, this velocity is sufficiently high enough to cause particle fracture on impact.

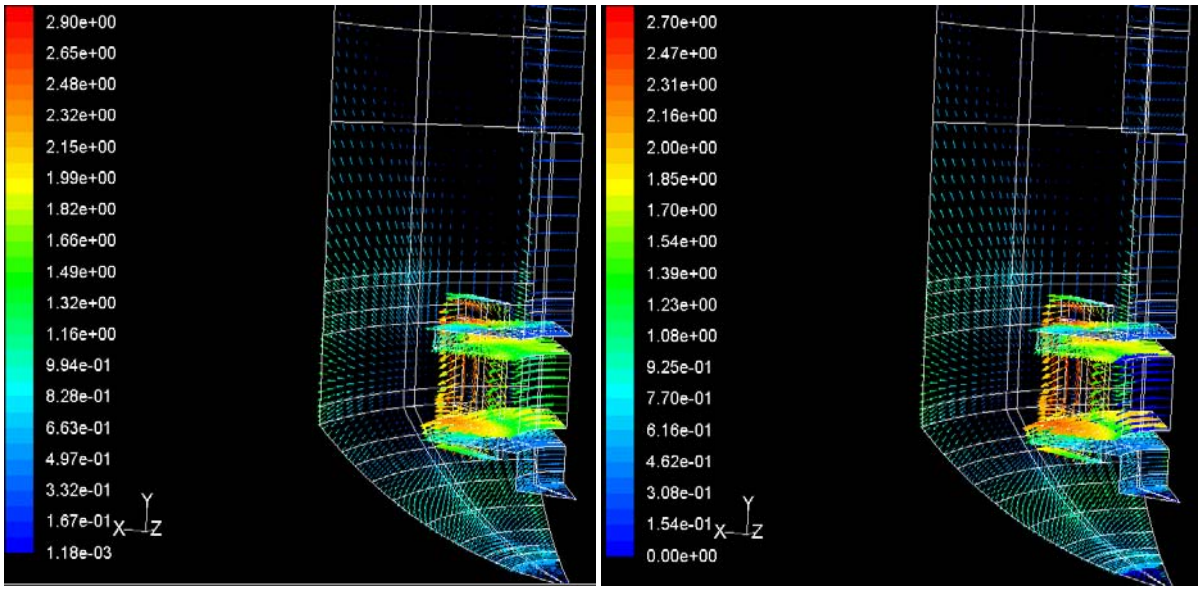

(a) (b)

Figure 19: *Absolute velocity vectors of (a) water and (b) olivine at t=2 seconds for 37μm case, values in m/s (dt=5.56e-4 seconds)*

Figures 19(a) and 19(b) indicate the vectors of absolute velocity of water-CO_2 aqueous mixture and olivine respectively within the reactor at t=2 seconds for the 37μ case. An interesting observation here is the difference in velocity magnitude of the olivine particles and the water-CO_2 mixture. The velocity profile of olivine follows the velocity profile of water closely; however, the velocity magnitude of olivine particles are observed to lag the corresponding values for the water-CO_2 mixture. It however remains to be seen if this effect is reflected in the 150μ case where the particle inertia is higher than the 37μ particles. Simulations are currently in progress for the 150μ case. During the first project year they have not yet progressed sufficiently in time to make a similar comparison.

37mu_phase_distro.wmv

Movie 1: *Movie depicting movement of the olivine phase in the ASU minireactor for the 37μ case (Double click to start). Contour values (in fraction) dynamically change as time progresses.*

Volume fraction distribution of the 37μ particles for 0.84 seconds of paddle wheel rotation (corresponding to 21 revolutions) is presented as a movie file (Movie 1). The movie file highlights the motion of the olivine phase when subjected to the agitation imposed by the impeller. This movie was generated by taking snapshots of volume fractions as the simulations progress at different time intervals. These snapshots were then combined to generate a movie

file. Generally throughout the simulation, the rotation of the paddle causes movement of the olivine particles within the reactor. These olivine particles are then forced upwards due to the high speed of the paddle blades, which causes a swirling motion within the reactor. As the olivine is dispersed throughout the reactor, the initial volume packing fraction of 63% reduces dramatically. This reduction is relatively gradual in its initial stages and the effect is seen on the level which is displayed as a color bar on the left. A swirling motion is observed and this is consistent with the velocity vector plots shown in Figures 18a-c.

Generally throughout the simulation, the rotation of the paddle causes gradual movement of the olivine particles along the direction of the paddle rotation. These olivine particles are then carried upwards entrained in the fluid flow associated with the high speed of the paddle blades, which also induces a swirling motion within the reactor, as observed in Movie 1. Analysis of the structural features of the flow in the minireactor as well as the statistics associated with the olivine volume fraction and velocity distributions for the different size fractions are of key interest for enhancing particle abrasion, passivating layer exfoliation and mineral carbonation. The objective is to engineer cost-effective reaction flow dynamics that enhance particle abrasion via particle-particle and particle-vessel interactions, which in turn enhance passivating layer exfoliation and carbonation.

During the no-cost extension, we are continuing to carry out simulations using much smaller time steps than in the initial runs, time steps that correspond to a paddle wheel rotation of approximately 5 degrees per step. To shorten the associated computational time required to complete the analysis, we have purchased three additional licenses for the Fluent code to be utilized during the no-cost extension period. To verify the accuracy of these simulations, we are currently constructing a transparent plexiglass reaction vessel for the minireactor to perform experiments using water-olivine slurries at ambient temperature and pressure and 1500 rpm stirring. Visualizations of the slurries will be compared to the flow dynamics predicted by the CFD model to further assess the model's validity.

Scientific Progress: Investigation of the Potential that Sonication Offers to Enhance Exfoliation and Carbonation

As during the first year investigations, the second year sonication experiments were carried out by stopping the standard mineral carbonation reaction after a half hour, introducing a brief sonication period, and following with a second half-hour exposure to the standard aqueous mineral carbonation process. The overall carbonation reaction conditions remained the same as the standard carbonation conditions throughout the two half-hour mineral carbonation steps. Extent of carbonation runs that mimic the sonication runs, but without the intermediate sonication exposure, were again used for baseline comparison. In each case 10 or 20 g of <38μ or <75μ San Carlos olivine was mixed with 50ml or 75ml of the standard aqueous solution (1M NaCl + 0.64 M $NaHCO_3$) and added to the batch reaction system. After 30 min of stirred reaction under the standard conditions, the reaction was stopped and rapidly cooled by using the internal cooling coil and placing the reaction vessel in ice water. This results in the temperature dropping to ~40°C within 10 minutes. After cooling is complete, the system is depressurized and the batch reaction stirring system is replaced with the sonication system (Figure 20). The system

is purged with CO_2 and subsequently brought to the starting sonication temperature and pressure. Once at temperature and pressure, sonication is then run for controlled periods of time. Once sonication is done, the vessel rapidly cooled in ice water and then depressurized. The vessel containing the reaction mixture is next reattached to the batch reaction system and the second half-hour carbonation step is performed.

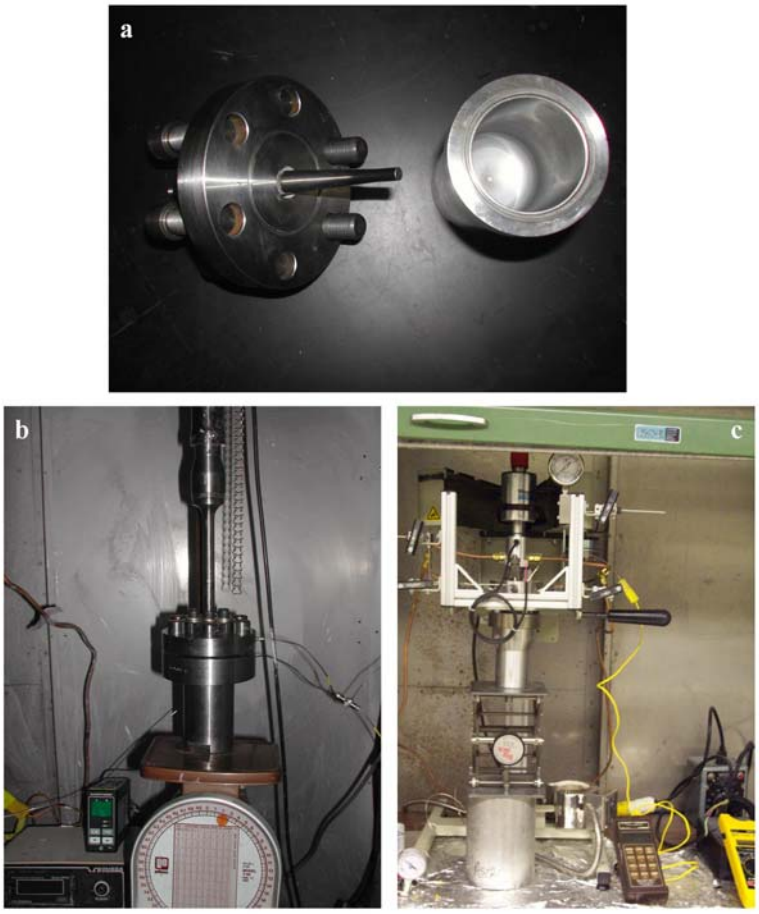

Figure 20: *The sonication and batch reaction systems at Arizona State University: (a) The sonication probe and reaction vessel; (b) the reaction vessel sealed to its sonication assembly; (c) the same reaction vessel shown in a and b sealed to the batch reactor stirring assembly.*

During the first project year, the effects of full-power sonication on the extent of carbonation were explored as a function of sonication time, temperature and pressure (1 to 10 minutes; 20 to 185 ^{o}C; 15 to 2,200 psi CO_2) . Under none of the conditions investigated did the sonication process enhance carbonation. Given that the extent of carbonation varies by as much as ±5% for the same reaction conditions in these studies, the results suggest that sonication may even inhibit carbonation. This suggests that full-power (1500 watt) sonication may significantly reduce carbonation.

During the second project year, the effects of sonication on the extent of carbonation were explored at reduced power, as the full-power investigations carried out during the first year did not show any indication that full-power sonication could enhance carbonation, let alone enhance

it cost effectively. Studies were carried out as a function of the weight % olivine present, the olivine particle-size distribution, the volume fraction of the aqueous solution present, and sonication power, time, temperature, and CO_2 pressure. Representative results are shown in Table 1 below. None of the conditions investigated to date have significantly enhanced carbonation. Indeed, many of the conditions employed appear to inhibit carbonation. As sonication is relatively costly (energy intensive) compared with the other two approaches being investigated (aqueous chemistry and slurry-flow control) and has not shown promise for low-cost enhancement of carbonation, the other two approaches will be primarily explored during the no-cost extension period.

Table 1: Effect of Sonication on the Extent of San Carlos Olivine Carbonation

Exp #	Particle Size	Mass (g) Olivine	Sonication Conditions	*Extent of carbonation**
303	<38μ	10	1min, 185 °C, 2200psi CO_2, 40% power	**8.16**
304	<38μ	10	no sonication	**31.14**
305	<38μ	10	1min, 100 °C, 2200psi CO_2, 40% power	**9.20**
306	<38μ	10	1min, 100 °C, 900psi CO_2, 40% power	**10.39**
307	<38μ	10	1min, 100 °C, 900psi CO_2, 30% power	**13.55**
308	<75μ	10	1min, 100 °C, 900psi CO_2, 40% power	**4.40**
309	<38μ	20	1min, 100 °C, 900psi CO_2, 40% power	**29.08**
310	<38μ	10	5min, 100 °C, 900psi CO_2, 40% power	**22.19**
311	<38μ	10	1min, 100 °C, 900psi CO_2, 40% power	**18.48**
312	<38μ	10	1min, 20 °C, 900psi CO_2, 40% power	**32.91**

* The carbonation reaction conditions are: standard solution of 0.64M $NaHCO_3$ + 1.00M NaCl for ½ hour at 185 °C, 2200psi CO_2 and stirring at ~1500rpm using 50ml of aqueous solution. The only difference is for #311, which used 75ml, instead of 50ml of aqueous solution for both the carbonation and sonication steps. In each case, carbonation is carried out for 30 minutes before and after the above sonication exposures. The run that did not incorporate sonication (#304) replicated the two 30-minute carbonation runs for each of the sonication runs, including the cooling and depressurization cycles between the two 30-minute carbonation runs.

Figure 21 shows typical field emission scanning electron microscopy (FESEM) secondary electron images of partially reacted olivine particles after the three primary stages of the sonication process: after ½ carbonation, after ½ hour of carbonation followed by sonication, and after ½ hour of carbonation, sonication and a second ½ hour of carbonation. Interestingly, all the particle surfaces show similar surface bound silica-rich passivating layers and magnesite crystals for the particles observed, indicating that sonication is not effective at enhancing passivating-layer exfoliation or breaking the olivine feedstock into smaller olivine particles. Why sonication appears to inhibit carbonation in many cases is not well understood and is being investigated during the no-cost extension.

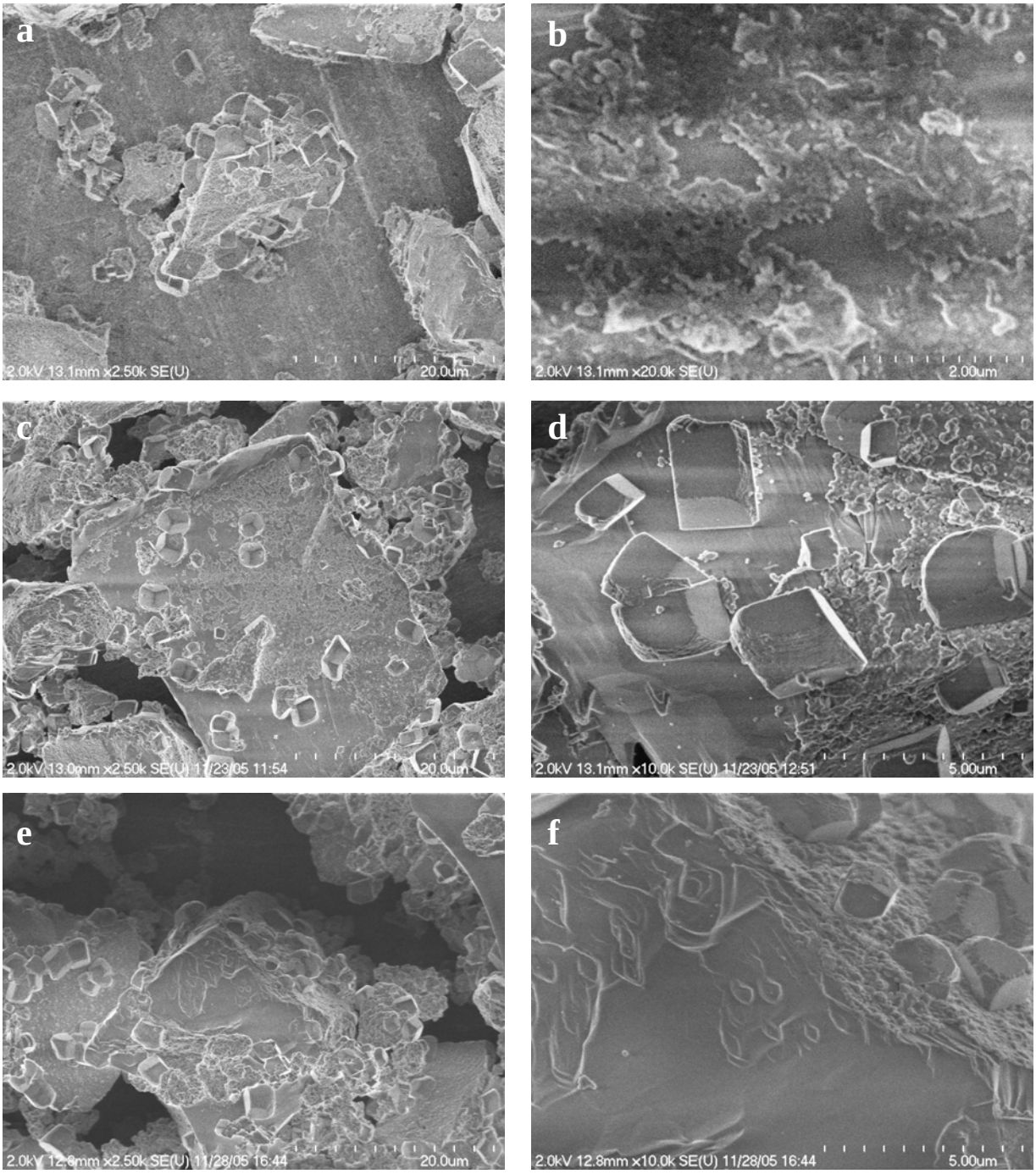

Figure 21: *Field emission scanning electron microscopy secondary electron images showing the surface morphology of the partially reacted/carbonated olivine grains: (a) & (b) after ½ h carbonation, but before sonication; (c) & (d) after ½ h carbonation and one minute of sonication at ambient temperature under 15 psi CO_2 ; (e) & (f) after ½ h reaction/carbonation, one minute of sonication at ambient temperature under 15 psi CO_2,, and a second ½ hour of reaction/carbonation under the standard conditions.*

Scientific Progress: Understanding the Mechanisms that Control Passivating Layer Formation and the Impact the Above Approaches Have on Exfoliation and Carbonation Mechanisms

During the second project year, we have evaluated the effectiveness of a variety of reaction flow dynamics, alkali cation solution chemistry, and sonication approaches to enhance carbonation. These studies have involved carbon elemental analysis and X-ray powder diffraction of many scores of product samples. The primary objective is to identify those approaches that are most effective in enhancing carbonation. Our mechanistic investigations have substantially focused on enhancing our understanding of passivation layer structure, composition and behavior. The objective is to enhance our fundamental understanding of the passivating-layer formation, growth and exfoliation process, while we are exploring in parallel the impact that reaction flow dynamics, alkali cation solution chemistry, and sonication have on exfoliation/carbonation. During the no-cost extension, we will explore the impact that the approaches that are identified as being most effective in enhancing carbonation have on the mechanisms that govern passivation layer formation, properties, exfoliation, and carbonation reactivity. Substantial progress has been made in enhancing our understanding of passivating layer formation processes during the second project year. A substantial amount of our progress during the first and second project years is summarized in our recent publication of a comprehensive paper describing the silica-rich passivating-layer formation, growth, and exfoliation processes that accompany olivine mineral carbonation. This article emphasizes our mechanistic observations associated with stirred carbonation. As a copy of this article is included in Appendix A,[17] the associated progress will not be repeated here. Additional studies carried out during the second project year are described below.

Overview of the feedstock incorporated: Olivine forms a solid solution series between its end members forsterite (Mg_2SiO_4) and fayalite (Fe_2SiO_4), with naturally occurring olivine generally richer in magnesium.[18] It adopts an orthorhombic structure, with Mg and Fe interchangeably occupying the same lattice sites. The cell parameters generally increase with increasing Fe content, exhibiting Vegard-like behavior between the forsterite and fayalite end members (e.g., Mg_2SiO_4: a = 4.76Å, b = 10.20Å, and c = 5.98Å; Fe_2SiO_4: a = 4.82Å, b = 10.48Å, c = 6.11Å).[18] The single crystal San Carlos olivine fragments used in the following investigation of the mechanisms that control carbonation at the aqueous solution/olivine reaction interface contain ~8.5% Fe - $(Mg_{0.915}Fe_{0.085})_2SiO_4$.

Mechanistic Observations Associated with the Static Aqueous Carbonation Process. Investigation of passivating-layer formation and growth processes under static, rather than stirred, conditions offer the opportunity to explore the formation and growth behavior in the absence of particle abrasion and passivating-layer exfoliation. Our mechanistic observations associated with the stirred aqueous mineral carbonation process indicated that a silica-rich passivating layer forms on the olivine surface during carbonation. FESEM imaging, energy-dispersive X-ray analysis, X-ray diffraction analysis, elemental analysis and auxiliary techniques identified the olivine carbonation reaction products as amorphous silica and magnesium carbonate, along with residual unreacted olivine and established the extent of the reaction. However, the character of the reaction interface and the passivating-layer formation process were clouded by particle abrasion that is inherent in the rapidly stirred carbonation process. In order to gain greater insight into the passivating-layer formation and growth process, we

undertook experiments using oriented single crystal San Carlos olivine specimens in the standard carbonation environment applied by the Albany Research Center (aqueous solution containing 1.00M NaCl and 0.64M $NaHCO_3$ at 185 ^oC under 2,200 psi CO_2 pressure), but without stirring in order to preserve the passivating layer and the associated reaction interfaces that form. We then examined the passivating layers and the reaction interfaces using various high resolution electron microscopy (HREM) methods, secondary ion mass spectroscopy (SIMS), and auxiliary methods.

High-resolution transmission electron microscopy (HRTEM) results, some of which were reported earlier, showed that a silica-rich amorphous reaction layer, referred to herein as a passivation layer, had formed on the olivine surface during the carbonation reaction under the conditions noted above. A HRTEM image of the passivating-layer/olivine particle core interface region is shown in Figure 22. The passivating layers observed routinely contain a dispersion of magnesium carbonate nanocrystals, which have been identified as $MgCO_3$ (magnesite) by image analysis and Fourier nanodiffraction, as discussed in our first year progress report. The subsequent application of Fresnel and STEM annular dark field imaging methods during the second year of the project did not identify additional chemical or structural heterogeneitities in the passivating layer, and in particular, in the passivating-layer/olivine interface region. Interestingly, the intervening equilibrium phase between SiO_2 and forsterite is enstatite, but this phase was not observed providing further support that magnesium dissolution and carbonation results in direct silica formation. Apparently, the CO_2 that results in the high CO_2 activity in the aqueous solution also penetrates the silica-rich passivating layers that form, leading to the formation of magnesite within, as well as external to the passivating layers.

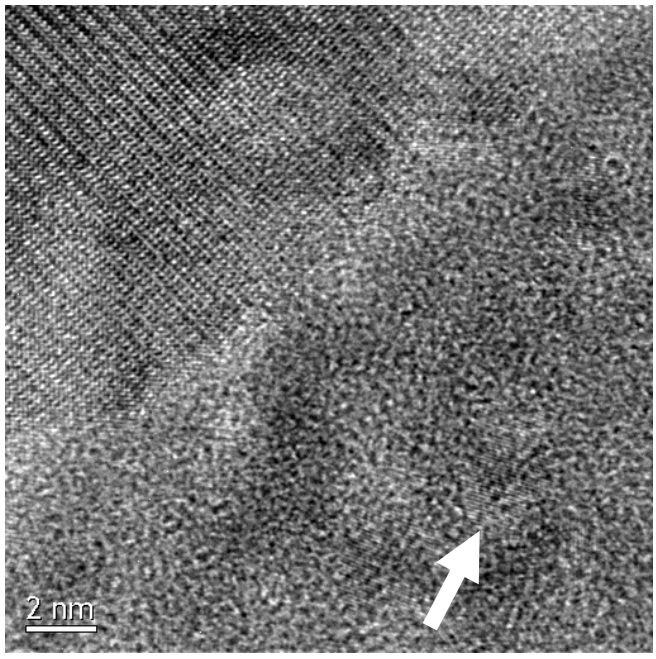

Figure 22: *HRTEM cross section image of the well-bonded interface between olivine and the passivating layer, (4h carbonation at 185 ^oC under 2,200 psi CO_2). The host olivine is at the upper left. The passivating layer is ~40 nm thick. The arrow on the image points to a typical $MgCO_3$ nanocrystal in the amorphous passivating layer matrix.*

HRTEM methods were used to determine how broadly applicable our first year observation that the $MgCO_3$ volume fraction in the passivating layer was about 13% is. An average of 14% was observed for various specimens/regions during the second year. Electron energy loss spectroscopy was then incorporated to determine the low loss peak energy of the passivating layer, which was 23±1 eV in good agreement with the value for SiO_2;[19] core edge analysis indicated that the O/Si ratio was slightly less than 2, confirming the carbonation reaction of interest both at the reaction interface and overall can be best described as:

$$Mg_2SiO_4 + 2CO_2 = SiO_2 \bullet 2MgO + 2CO_2 = SiO_2 + 2MgCO_3 \qquad (2)$$

Using reaction 2 and the known molar volumes of the products and reactants, which are 43.6, 28.0, and 26 cc/mol for olivine, $MgCO_3$, and amorphous SiO_2, respectively,[20] the calculated expected volume fraction $MgCO_3$ in the reaction product layer is ~ 67%, which is far greater than the amount observed. The balance of the magnesite was found to reside in the trace reaction residue that was found at the bottom of the reactor. Post-reaction X-ray diffraction and elemental (PIXE) analysis of the residue collected from the bottom of the reaction pressure vessel showed the presence of magnesite, smaller amounts of amorphous SiO_2, and still less olivine, confirming the conclusion that most of the $MgCO_3$ formed external to the passivating layer itself. $MgCO_3$ nanocrystals were never observed in the olivine itself, indicating that CO_2 penetrates the passivating layer up to, but not beyond, the passivating-layer/olivine reaction interface during carbonation. This is consistent with a relatively high concentration of $Mg^{2+}$and O^{2-} forming near the interface, which is available to react with the in-diffusing CO_2 to form the $MgCO_3$ nanocrystals observed. The relatively low concentration of $MgCO_3$ nanoparticles in the passivating layer indicates that they nucleate inhomogeneously; however, the character of the preferred nucleation sites is not clear at present.

As discovered in the first project year, the olivine surface reacted under static conditions exhibits a silica-rich sponge-like morphology, as shown in the left of Figure 23. Sonication of the as-reacted surface in aqueous media exposes the underlying cracked silica-rich surface morphology shown in the right of Figure 23. Energy dispersive x-ray spectroscopy showed that the passivating-layer regions for both unsonicated and sonicated specimens were silica rich, while the areas at the bottom of the fractures in the sonicated passivating layers corresponded to olivine. Although the former result is not quantitative, as the incident electron beam penetrated through the passivating layer and the x-ray emission volume included regions of passivating layer and the underlying olivine, qualitative observations from multiple samples have clearly established that the passivating layers seen in Figure 23 are silica-rich, in agreement with the above analytical HRTEM observations.

The complex morphology of the curled-up silica-rich surface structure of the passivating layer shown in the left of Figure 23 is not entirely due to the stress system developed in the near-surface region of the specimen, which is discussed below. Part of this morphology is also due to the solubility of SiO_2 in neutral to slightly acidic water with a pH very similar to the aqueous solution incorporated herein (pH ~ 6.85; See Appendix A).[17] Several investigators have shown that small amounts of amorphous SiO_2 will dissolve in neutral to slightly acidic water,[21,22] and the presence of aqueous NaCl can enhance the dissolution kinetics.[23]

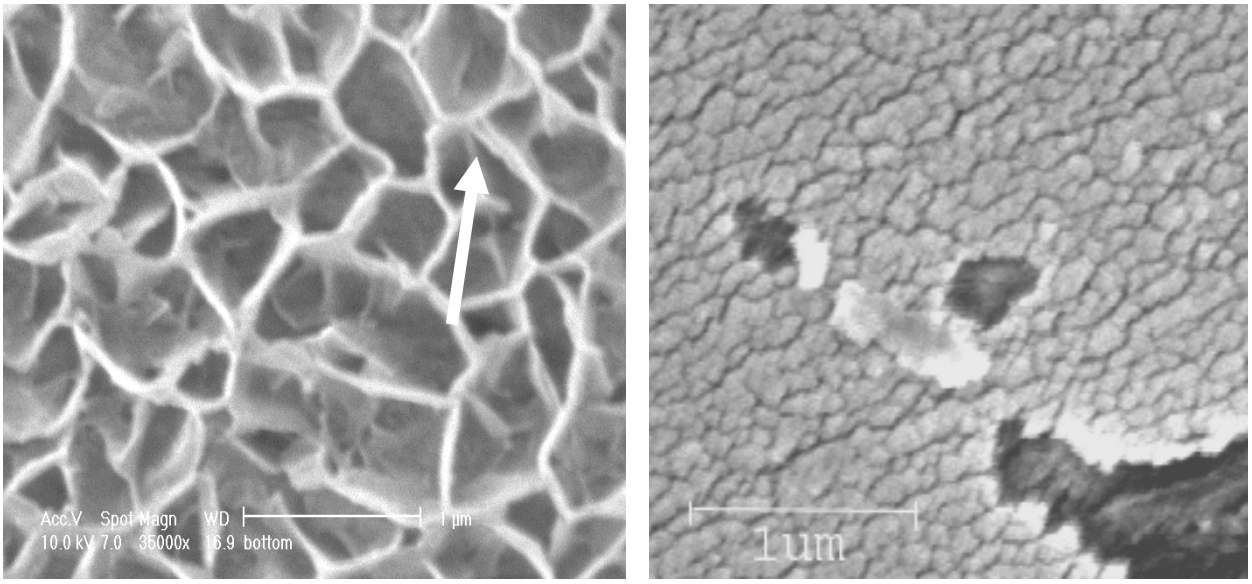

Figure 23: *FESEM images (secondary electron) of the olivine surface after reaction for 4 hours at 185 ^{o}C under 2,200 psi CO_2. The left image, recorded before sonication, shows the sponge-like character of the silica-rich passivating layer that has curled up/grown away from the olivine reaction interface. One region where two curled up pieces are separated by a narrow crack is highlighted by the arrow. The right image, after sonication, shows that the curled passivating-layer structure is removed by sonication to reveal the underlying fractured, silica-rich island-like structure shown. Some of the silica-rich islands have broken away from the surface to reveal the underlying olivine- rich crystal core.*

Hence, the amorphous silica that forms during carbonation can exhibit significant mobility via the aqueous phase and be transported via dissolution-precipitation.

The possible role of hydrogen/water within the passivating layers during carbonation is of substantial interest, as proton/Mg^{2+} exchange may occur with water formation near the olivine/passivating-layer interface during olivine dissolution/carbonation. Several investigators have shown that small amounts of water molecules can dissolve and diffuse in SiO_2, forming SiOH groups in the process. The possible sites for such silanol formation are associated with dangling silicon or oxygen bonds in the network or on glass surfaces. For example, SiOH has been shown to form easily at dangling bonds on amorphous silica fracture surfaces.[24] There are several possible locations for high concentrations of dangling bonds in the passivating-layer/interface regions during carbonation, including free surfaces, vertical cracks that penetrate the passivating layer, and within the passivating layer itself, through which the aqueous carbonation species can diffuse.

In order to better understand the potential roles that $2H^{+}/Mg^{2+}$ exchange and water diffusion play during passivating-layer formation and carbonation, we explored the passivating-layer/olivine surface reaction region using O^{+} SIMS profiling. An example of the results for a sonicated passivating-layer reaction surface are shown in Figure 24. A layer of Si was deposited by e-beam

evaporation under UHV prior to SIMS analysis of the surface, to establish a steady state SIMS profiling rate before beginning to analyze the passivating-layer region. The initial rise of the Si curve is due to the Si cap layer. Analysis of the surface of the passivating layer begins at the left side of the slat Si maximum. Note that the H curve exhibits a maximum at the beginning of the passivating layer, and then a secondary maximum near the passivating-layer/olivine interface. The position of the interface is defined by the steep rise of the Mg curve and the drop in the Si curve from its value in the passivating layer to its lower value in the olivine matrix. The moderate slopes of these curves result from oxygen ion beam induced mixing during the experiment, which is a common feature of any sputter depth profiling procedure. The two most important conclusions to be drawn from our SIMS results are that hydrogen did diffuse through the passivating layer during carbonation, and the resulting hydrogen distribution, likely associated with SiOH formation, is enhanced near the passivating-layer surface and the passivating-layer/olivine interface. Hydrogen diffusion through the passivating layer during carbonation is consistent with proton/Mg^{2+} exchange occurring near the olivine/passivating-layer interface during olivine dissolution/carbonation. It is also probable that SiOH groups form on the vertical crack surfaces associated with the passivating-layer, as shown in the right side of Figure 23. Future studies are planned using a sputter-deposited gold capping layer to more quantitatively resolve the composition of the near-surface region of the passivating layer.

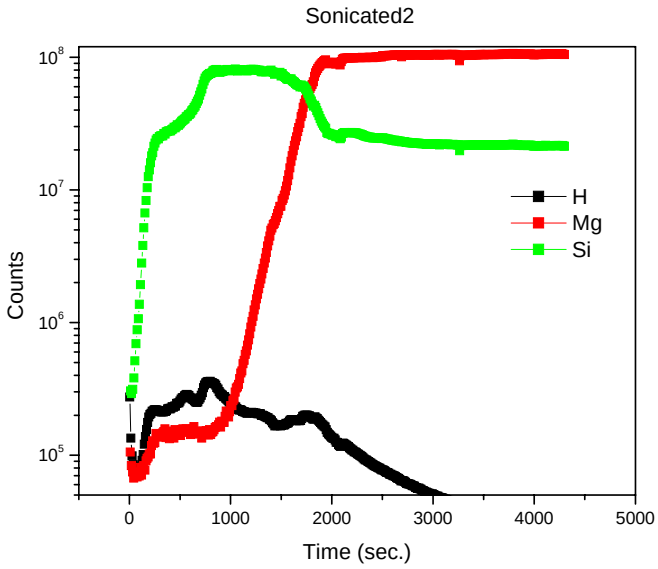

Figure 24: *SIMS depth profiles for H, Mg and Si for the surface of a sonicated passivating-layer region of a sample after a 4 h static reaction. The free surface is at left, and the olivine substrate is at right.*

The strains responsible for the cracking and exfoliation of the passivating layers are due to transformation strains that occur when the olivine rejects Mg and O during its transformation to amorphous SiO_2. From the molar volumes summarized as a function of magnesite content within the passivating layers in Table 2, it is clear that the passivating layers that form are in a state of biaxial tension. The calculated stress is quite large because the molar volume difference between

Table 2: Molar Volume of the Passivating Layer Region (Products) Compared to Host Olivine (Reactants) as a Function of the Volume of Magnesite Nanocrystals within the Passivating Layer.

%$MgCO_3$ In layer	V(products) / V(reactants)	Strain State of layer	$MgCO_3$ % Volume in layer
100%	1.91	*compression*	67%
90%	1.78	*compression*	65%
80%	1.65	*compression*	62%
70%	1.52	*compression*	59%
60%	1.39	*compression*	55%
50%	1.26	*compression*	51%
40%	1.13	*compression*	45%
30%	1.01	*compression*	38%
20%	0.88	*tension*	29%
10%	0.75	*tension*	17%*
0%	0.62	*tension*	0%

* HRTEM

olivine and SiO_2 is large; the presence of the small $MgCO_3$ particles observed via HRTEM only partially offsets the induced stress as their volume fraction is relatively small. Most of the passivating layer "islands" observed between the vertical cracks, easily visible in the right of Figure 23, are strongly bonded to the olivine substrate, as shown by the images of their interfaces (e.g., Figure 22). The bond at these interfaces creates a strain gradient in the passivating layer, from the olivine interface up to the free surface. The strain gradient induces shear stresses and normal, peeling, stresses at the interface between the olivine and the passivating layer. These are similar to misfit stresses between a thin film and its substrate induced by differential thermal contraction, when a film/substrate combination is cooled from its deposition temperature.[25,26] However, in the present case the stresses are associated with the transformation strain induced by the differences in molar volume, not differential thermal contraction, which, in turn drive the passivating-layer cracking/exfoliation process.

A model that is consistent with the passivating-layer cracking process is shown in Figure 25. Initially the passivating layer forms as a thin film on the olivine single crystal surface. As it thickens, biaxial tensile stress causes cracks through the layer. Then bending moments and interface shears can lead to exfoliation and detachment. As these events occur, new secondary passivating-layer formation can begin associated with the newly exposed olivine surfaces. The presence of water-induced silanol formation may impact the fracture/exfoliation process, as silanol groups are thought to reduce the surface energy of Griffith cracks in glass by forming at crack tips as they propagate.[27,28] This should enhance the fracture/exfoliation process under our experimental conditions. It is important to note the large relief of the unsonicated silica-rich passivating layer structure in the left of Figure 23. Such high features are not possible via passivating layer bending away from the olivine interface alone. Indeed, it appears that silica

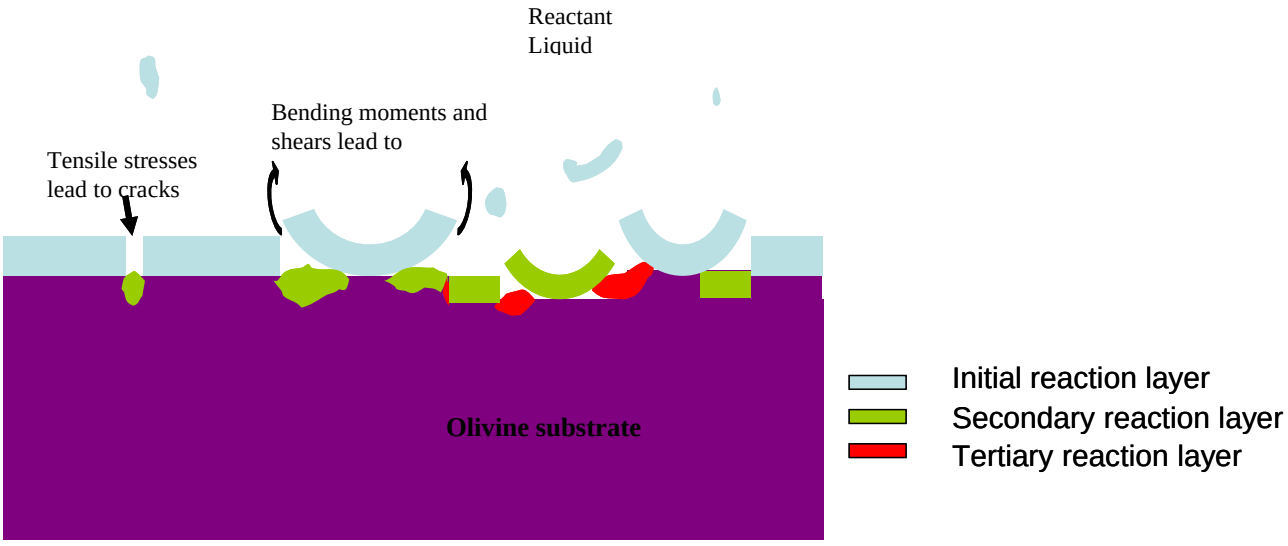

Figure 25: *A possible model of the passivating layer formation and fracture process, which is combination with silica dissolution/precipitation, may lead to the silica-rich passivating-layer surface features observed in the left of Figure 23.*

dissolution/precipitation plays a significant role in the passivating layer formation and growth process observed under static reaction conditions. Close examination of the surface structures in the left of Figure 23 are consistent with (1) silica dissolution being able to occur at the base of and along passivating-layer cracks that extend to the olivine interface and (2) silica precipitating along the vertical silica-rich passivating layer structure as it diffuses away from the passivating-layer/olivine interface. Such a process allows for the growth of silica-rich structures away from the interface, as observed in the left of Figure 23.

Scientific Progress: Simulations of Reactant Solutions

As discussed above, we found that reactions carried out in high concentration bicarbonate solutions (e.g., $KHCO_3$ and $NaHCO_3$) significantly enhance carbonation. However, at the highest bicarbonate concentrations we routinely observe a slight but systematic decrease in carbonation, which may be related to the solubility behavior of CO_2(aq) at high pressures and temperatures. Unfortunately, the experimental phase diagram for this system at the conditions of interest is currently not available. Therefore, to gain some preliminary insight we have calculated the solubility of CO_2 over the range P_{CO2} = 20–160 bar and T = 10–200 ^oC in the presence/absence of NaCl using a highly quantitative model recently introduced by Duan at al.[29] Currently this model is limited to the incorporation of Na^+, K^+, Mg^{2+}, Ca^{2+}, Cl^- and SO_4^{2-} species in an H_2O-CO_2 solution. Some representative results for H_2O-CO_2 and H_2O-CO_2-NaCl are provided in Figure 26 below, which shows the temperature dependence of the CO_2 solubility for a range of isobars.

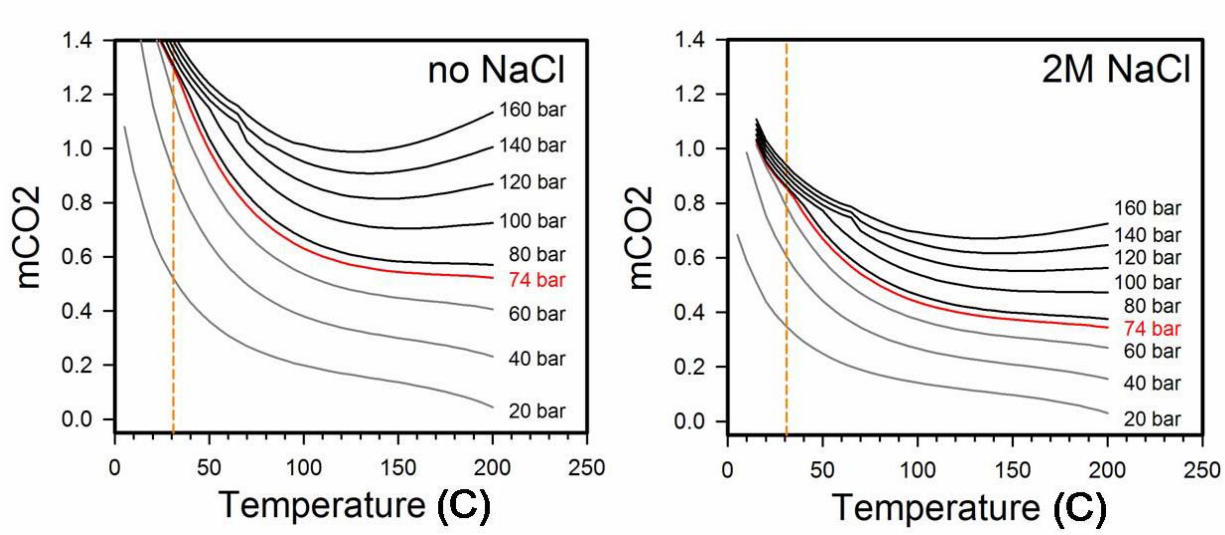

Figure 26: *Calculation of CO_2 solubility in H_2O without and with the presence of 2M NaCl.*

The calculations indicate the addition of NaCl substantially reduces CO_2 solubility in general, as expected. However, while the solubility decreases with increasing temperature for pressures below 74 bar, a minimum is observed near 130 ^oC at high pressure. Thus, for example, in a 2M NaCl solution the solubility of CO_2 at 160 bar is expected to be the same (~ 0.73M) at 83 ^oC and 200 ^oC. Importantly, the above results indicate that the addition of NaCl to saturated aqueous solutions of CO_2 can substantially decrease the activity of CO_2(aq) present. During the no-cost extension, we plan to explore to what extent these findings extend to the presence of $NaHCO_3$ vs. NaCl in the aqueous solution.

CONCLUSIONS

Robust silica-rich passivating layers have been discovered to form on the olivine surface during mineral carbonation. These passivating layers thicken, fracture and exfoliate during rapidly-stirred carbonation, exposing fresh olivine surfaces that enhance carbonation reactivity. Aqueous carbonation reactivity is a strong function of (1) the ionic species present, (2) their aqueous activities, and (3) the slurry flow conditions present during carbonation. The most effective carbonation solutions to date are high concentration sodium, potassium, and sodium/potassium bicarbonate aqueous solutions. The most effective of these solutions (5.5M $KHCO_3$) has been found to nearly double the extent of carbonation observed using the standard aqueous solution developed by the Albany Research Center. High concentration aqueous bicarbonate solutions have also been found to preferentially enhance the relative carbonation reactivity of olivine containing larger particle-size fractions (e.g., <75µ and <150µ vs. <38µ). Being able to effectively carbonate olivine feedstocks containing such larger particle-size fractions offers the potential to substantially reduce feedstock grinding cost and lower mineral sequestration process cost.

Slurry-flow dynamics have been found to be a strong function of particle size and mass via macroscopic simulations using Fluent, suggesting that controlling these parameters may offer

substantial potential to enhance passivating-layer abrasion/exfoliation and carbonation. Synergistic control of the slurry-flow and aqueous chemistry parameters incorporated during carbonation appears to offer the best potential to further improve carbonation reactivity for unactivated olivine feedstock materials.

During the second project year we improved the design of the sonication exfoliation system developed during the first year and extended our investigations of the effects sonication can have on the extent of carbonation as a function of particle size distribution, the mass of solid reactant, volume fraction of aqueous solution present, sonication power, time, temperature, and CO_2 pressure. None of the conditions investigated have significantly enhanced carbonation.

Aqueous olivine carbonation involves both incongruent magnesium dissolution and silica precipitation, which result in robust silica-rich passivating layer formation. Secondary ion mass spectrometry investigations of the H content and profile within the passivating layers suggests $2H^+/Mg^{2+}$ ion exchange is associated with incongruent dissolution. These observations are consistent with H_2O forming at or near the olivine/passivating-layer interface within the passivating layer during the carbonation process. After forming, the water diffuses out through the passivating layers during the carbonation reaction. Together with the observation that magnesite nanocrystals form within the passivating layers during carbonation, this indicates that the passivating layers offer substantial permeability to the key solution reaction species present during carbonation (e.g., Mg^{2+}, H^+, H_2O, CO_2, and HCO_3^-).

Substantial tensile stress builds in the passivating layers and at the passivating-layer/olivine interface associated with the dramatic volume decrease as olivine forms silica at the reaction surface. This stress facilitates passivating layer cracking and exfoliation. The importance of particle abrasion in enhancing carbonation reactivity was confirmed via the addition of quartz particles as an abrasive slurry, which significantly enhanced carbonation. Studies during the no-cost extension period will take full advantage of progress to date, further exploring the potential that the aqueous chemistry and slurry-flow dynamics associated with carbonation offer to enhance carbonation reactivity and reduce olivine mineral sequestration process cost.

REFERENCES

1) *Carbon Sequestration Research and Development*, Offices of Science and Fossil Energy, U.S. Department of Energy (December **1999**), and references therein.
2) Seifritz, W. *Nature* 345, 486, **1990**.
3) Lackner, K.; Wendt, C.; Butt, D.; Joyce Jr., E.; Sharp, D.; *Energy* **1995,** 20, 1153-70.
4) O'Connor, W., et al. *Proc. 25th International Technical Conference on Coal Utilization & Fuel Systems* **2000,** pp. 153-64,.
5) O'Connor, W.K., et al. *Proc. 27th International Technical Conference on Coal Utilization & Fuel Systems* **2002** pp. 819-30.
6) *Novel Approaches to Carbon Management* (National Academies Press, Wash. D.C., **2003**)
7) O'Connor, W.K.; Walters, R.P.; Dahlin, D.C.; Rush, G.E.; Nilsen, D.N.; Turner, P.C.; *Proc. 26th International Technical Conference on Coal Utilization & Fuel Systems* **2001,** 765.

8) O'Connor, W.K.; Dahlin, D.C.; Rush, G.E.; Gerdemann, S.J.; Penner, L.R. *Proc. 29th International Technical Conference on Coal Utilization & Fuel Systems* **2004,** 71.
9) Yu, S.C.; Proc. Nat. Sci. Counc. A. ROC, **1997,** 21, 173.
10) Ottonello, G.; Princivalle, F.; Della Giusta, A.; *Phys. Chem. Miner.* **1990**, 17, 301.
11) McKelvy, M.J.; Chizmeshya, A.V.G.; Soignard, E.; Marzke, R.; Wolf, G.; Béarat, H.; Doss, B. *Proc. 31st International Technical Conference on Coal Utilization & Fuel Systems* **2006** 1-17.
12) McKelvy, M.J.; Diefenbacher, J.; Chizmeshya, A.V.G.; Wolf, G.; G.; Marzke, R.; Béarat, H.. *Proc. 30th International Technical Conference on Coal Utilization & Fuel Systems* **2005,** 26, 265-79.
13) Launder, B.E.; Spalding, D.B. *Lectures in Mathematical Models of Turbulence*, Academic Press, London, England, **1972**.
14) Ding J.; Gidaspow, D. *AIChE J*., **1990**, 36(4):523-538.
15) Gidaspow, D.; Bezburuah, R.; Ding, J. *In Fluidization VII, Proceedings of the 7th Engineering Foundation Conference on Fluidization*, **1992**, pages 75-82.
16) Gidaspow, D. *Multiphase Flow and Fluidization* (Academic Press, Boston, **1994**).
17) Béarat, H.; McKelvy, M.J.; Chizmeshya, A.V.G.; Gormley, D.; Nunez, R.; Carpenter, R.W.; Squires, K. *Environmental Science & Technology* **2006,** 40, 4802-8.
18) Hurlbut, Cornelius, S.; Klein, Cornelis; *Manual of Mineralogy*, 19th Edition (John Wiley & Sons, New York, **1977**).
19) Skiff, W.M.; Carpenter, R.W.; Lin, S.H. *J. Appl. Phys* **1988,** 64(11), 6328-6335.
20) Kingery, W. D. et. al., **Introduction to Ceramics**, 2nd edition, John Wiley and Sons (**1976**).
21) Rimstidt, J.D.; Barnes, H.L. *Geochimcia et Comochimica Acta* **1980,** 44**,** 1683-99.
22) Alexander, G.B.; Heston, W.M.; IIer, R.K. *J. Phys. Chem.* **1954,** 58(6), 453.
23) Dove, P.M.; Crerar, D.A. *Geochimica et Cosmochimica Acta* **1990,** 54, 955-69.
24) D'Souza, A.D.; Pantano, C.G. *J. Amer. Ceram. Soc.* **1999,** 82(5), 1289-93.
25) Stoney, G.C. *Proc. Roy. Soc. London* **1909,** A82, 172.
26) Suhir, E. *J. Appl. Mech.* **1986**, 53, 657-60.
27) Chiang, Y-M., Birnie, D.; Kingery, W.D. *Physical Ceramics*, John Wiley & Sons (**1997**).
28) Doremus, R. H. *Glass Science*, 2nd edition, John Wiley & Sons (**1994)**.
29) Duan, Z.; Sun, R.; Zhu C.; Chou, I-M. *Marine Chemisty* **2006,** 98, 131-39.

APPENDIX

Environmental Science & Technology **2006,** 40, 4802-8.

Environ. Sci. Technol. **2006**, *40,* 4802−4808

Carbon Sequestration via Aqueous Olivine Mineral Carbonation: Role of Passivating Layer Formation

HAMDALLAH BÉARAT,[†] MICHAEL J. MCKELVY,*[,†,‡] ANDREW V. G. CHIZMESHYA,[†,‡] DEIRDRE GORMLEY,[‡] RYAN NUNEZ,[‡] R. W. CARPENTER,[†,‡] KYLE SQUIRES,[§] AND GEORGE H. WOLF[||]

Center for Solid State Science, Science and Engineering of Materials Graduate Program, Departments of Mechanical and Aerospace Engineering and Chemistry and Biochemistry, Arizona State University, Tempe, Arizona 85287

CO_2 sequestration via carbonation of widely available low-cost minerals, such as olivine, can permanently dispose of CO_2 in an environmentally benign and a geologically stable form. We report the results of studies of the mechanisms that limit aqueous olivine carbonation reactivity under the optimum sequestration reaction conditions observed to date: 1 M NaCl + 0.64 M $NaHCO_3$ at $T \approx 185$ °C and $P_{CO2} \approx 135$ bar. A reaction limiting silica-rich passivating layer (PL) forms on the feedstock grains, slowing carbonate formation and raising process cost. The morphology and composition of the passivating layers are investigated using scanning and transmission electron microscopy and atomic level modeling. Postreaction analysis of feedstock particles, recovered from stirred autoclave experiments at 1500 rpm, provides unequivocal evidence of local mechanical removal (chipping) of PL material, suggesting particle abrasion. This is corroborated by our observation that carbonation increases dramatically with solid particle concentration in stirred experiments. Multiphase hydrodynamic calculations are combined with experiment to better understand the associated slurry-flow effects. Large-scale atomic-level simulations of the reaction zone suggest that the PL possesses a "glassy" but highly defective SiO_2 structure that can permit diffusion of key reactants. Mitigating passivating layer effectiveness is critical to enhancing carbonation and lowering sequestration process cost.

Introduction

World energy consumption is growing exponentially, driven by the increasing global standard of living (*1*, *2*). Although a diverse portfolio of energy generation technologies is available, the world depends on fossil fuels for over 80% of its energy needs. Coal satisfies a large fraction of this demand because of its wide availability, high energy density, and low cost. Known reserves can satisfy global energy demands well into the next century if the environmental concerns associated with atmospheric carbon dioxide emissions can be overcome (*1*−*5*). As alternative energy technologies are unlikely to satisfy this demand in the foreseeable future (*1*−*3*), carbon sequestration provides an important option for mitigating emissions (*1*−*3*, *5*). Relatively inexpensive options to reduce emissions are available in the near term, including fuel switching (e.g., coal to gas), enhanced fossil fuel generation efficiency, renewable energy generation, and terrestrial sequestration. Although these options cannot address the expected magnitude of long-term emissions, they can buy time to develop large-scale technologies that can.

Candidate large-scale technologies (e.g., ocean, geological, and above-ground mineral sequestration) are the subject of intense research (*1*, *2*). Of these, above-ground mineral sequestration offers the advantage of CO_2 disposal in geologically stable and environmentally benign form (*2*, *4*−*9*). However, process cost reductions are needed. Cost-effectively enhancing carbonation reactivity is key to economically viable process development. Enhancing mineral carbonation is also desirable during geological (below-ground) sequestration as it can ensure long-term sequestration stability via formation of thermodynamically stable mineral carbonates. Carbonation also induces volume expansion of the mineral feedstock, suggesting controlled carbonation may be used to promote reservoir seal integrity—a current topic of great practical interest. Investigating and evaluating candidate technologies that incorporate mineral sequestration (above and below ground) are the primary focus of the CO_2 Mineral Sequestration Working Group, which is managed by DOE (Fossil Energy), and consists of members from the Albany Research Center (ARC), Argonne National Laboratory, Arizona State University, Los Alamos National Laboratory, and the National Energy Technology Laboratory.

Carbonation of olivine minerals (e.g., forsterite, Mg_2SiO_4) is a leading mineral sequestration process candidate (*6*, *9*). Deposits are sufficient to support regional implementation of above-ground sequestration (*9*). Their low cost (~$4−5/ton for mined and milled feedstock) and exothermic carbonation (reaction 1) provide potential for economically viable process development (*5*, *6*, *9*).

$$^1/_2Mg_2SiO_4 + CO_2 \rightarrow MgCO_3 + {}^1/_2SiO_2$$

Recent ARC studies indicate aqueous solution carbonation is promising (*6*, *9*). Even without special activation, 30−50% carbonation has been achieved in an hour for <37 μm olivine at 185 °C and 135 bar CO_2. Pretreatment via intense attrition accelerates carbonation to near completion at reduced pressures and temperatures. However, the activation cost is high (*9*). Economically viable process development requires novel approaches that enhance carbonation while bypassing costly mineral pretreatment. Better understanding the mechanisms that control carbonation reactivity is central to engineering lower cost processes. The aqueous olivine carbonation process has been explored down to the nanoscale with particular emphasis on the changes that occur at the olivine reaction surface/interface. Silica-rich passivating layer formation, fracture, and exfoliation govern carbonation reactivity. Novel approaches that enhance fracture and exfoliation will likely substantially lower process cost.

Experimental Section

Olivine, $(Mg_xFe_{1-x})_2SiO_4$, forms a solid solution series between its end members forsterite (Mg_2SiO_4) and fayalite (Fe_2SiO_4) with naturally occurring olivine generally richer in

* Corresponding author phone: (480)965-4535; fax: (480)965-9004; e-mail: mckelvy@asu.edu.
[†] Center for Solid State Science.
[‡] Science and Engineering of Materials Graduate Program.
[§] Department of Mechanical and Aerospace Engineering.
[||] Department of Chemistry and Biochemistry.

10.1021/es0523340 CCC: $33.50
Published on Web 06/15/2006

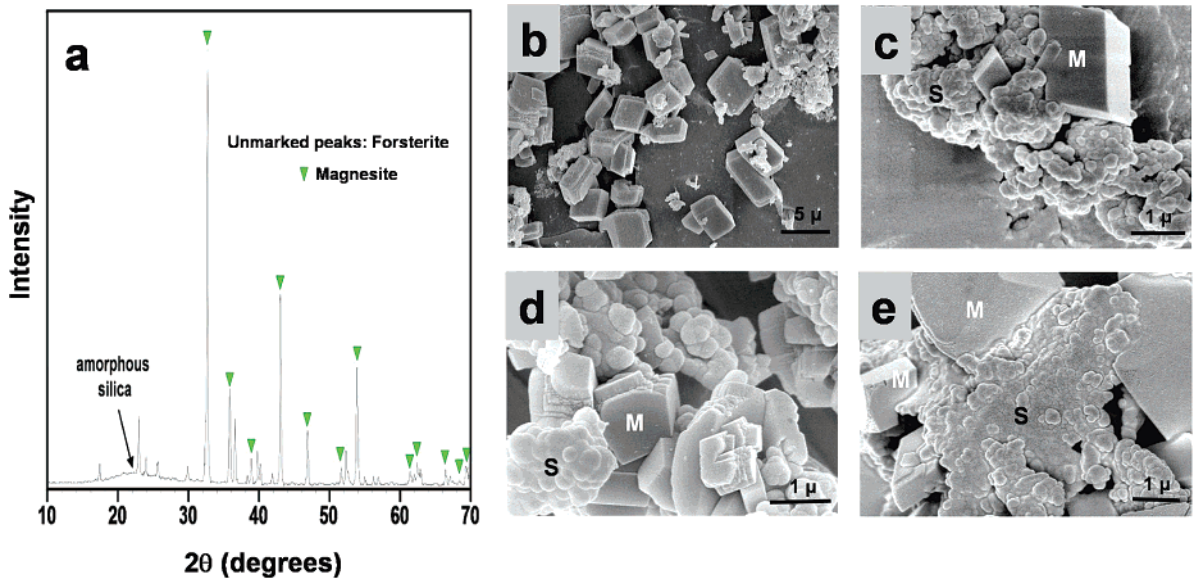

FIGURE 1. (a) XRD pattern of the olivine carbonation products. (b−e) FESEM of the magnesite crystals (M) and silica particles (S) that form during carbonation. Separate particles and crystals are frequently observed (b), but intergrowths are often observed as well (c−e). (d) Eroded magnesite crystal edges/corners are common (e.g., the crystal marked "M"), suggesting particle abrasion occurs during carbonation. (e) Intergrown silica/magnesite composite particle. Note the erosion of the outer edges of the softer magnesite crystals indicated by "M" indicating the composite particle formed during stirred carbonation (see also Figure 5).

magnesium (*10*). It adopts an orthorhombic structure with Mg and Fe occupying the same lattice sites. The cell parameters generally increase with increasing Fe content (e.g., Mg_2SiO_4: a = 4.76 Å, b = 10.20 Å, and c = 5.98 Å. Fe_2SiO_4: a = 4.82 Å, b = 10.48 Å, c = 6.11 Å) (*11*). Olivine from San Carlos, AZ, was used to explore the reaction surface/interface. Its composition $(Mg_{0.915}Fe_{0.085})_2SiO_4$ was determined using electron microprobe and particle-induced X-ray emission analysis. X-ray diffraction (XRD) showed the lattice constants are in good agreement with those for olivine containing ~8% Fe (a = 4.763 Å, b = 10.223 Å, c = 5.993 Å) (*12*). Trace impurities were well below 1%. Single crystals and their fragments were used to observe the olivine reaction surface/interface that forms during carbonation. Synthetic forsterite (Mg_2SiO_4) (99% Mg_2SiO_4; Alfa Aesar) was used for select investigations.

The optimum process to date for enhancing carbonation was developed by the Albany Research Center (ARC) based on extensive derivative investigations related to natural mineral weathering (*6*, *9*) and employed herein (185 °C, 135 bar CO_2, and aqueous 0.64 M $NaHCO_3$ + 1.00 M NaCl). Various particle sizes and reaction times were incorporated to probe the reaction/product materials vs reaction progression. 1500 rpm stirring further replicated the ARC process. The feedstock for the reaction surface/interface investigations contained equal weights of <37 and 37−200 μm single-crystal olivine fragments and occasionally a few larger (>200 μm) fragments. Mineral carbonation reactions were performed using an Autoclave Engineers EZE-Seal Hastelloy C-276 reactor.

The reaction products were analyzed structurally, morphologically, and analytically. XRD was obtained using a Rigaku D/MAX-IIB X-ray diffractometer with Cu Kα radiation. Scans were taken for 2θ ranges from 10° to 70° with 0.01°/s steps. A Hitachi S-4700 field-emission scanning electron microscope (FESEM) with energy-dispersive X-ray spectroscopy (EDS, Phoenix-EDAX) was used for imaging and analysis. Extent of carbonation and hydrogen content were assessed using a Perkin-Elmer Series II CHNS Elemental Analyzer. Comparative standards gave total carbon and hydrogen accuracies of ±0.3 wt %. Extent of carbonation observations were in good agreement with XRD product analysis.

Results and Discussion

Investigation of the Carbonation Reaction Products. XRD indicates aqueous carbonation produces magnesite, amorphous silica, and unreacted olivine (Figure 1a). The amorphous product is identified as a silica-like material by its characteristic broad scattering intensity around 22° 2θ (*13*). FESEM of the product materials reveal two characteristic particle shapes: (i) crystals and (ii) irregularly shaped product particles (Figure 1b−e). The crystals and particles are usually observed separately but are also found intergrown in clusters. The morphology of the irregular particles and the broad XRD intensity around 22° are consistent with hydrothermally formed amorphous silica (*13*). Detailed analysis of the scattering structure is needed to establish the associated short-range silica order and will be the subject of a future investigation. EDS confirms the irregular particles exhibit strong Si and O signals expected for silica and the polyhedral crystals exhibit the expected strong Mg and O signals for magnesite. Elemental analysis of the reaction products shows they do not contain H within experimental error (±0.3 wt %), indicating the silica-rich material is largely H free and primarily associated with Si−O−Si bonding (*14*).

Many magnesite crystals had irregular corners/edges (Figure 1d,e), indicating particle abrasion accompanies rapidly stirred (1500 rpm) carbonation. Abrasion can occur via particle−particle and/or particle−wall/impeller interactions. Intergrown magnesite/silica clusters were observed and typically exhibited preferential magnesite abrasion around the outer cluster edges, indicating they formed during stirred carbonation (Figure 1d,e). Intimate intergrowth of silica and magnesite indicates magnesite can nucleate/grow in association with silica formation as well as directly from solution.

Investigation of the Olivine Reaction Surface/Interface. Multiple reactions were stopped before completion to explore the olivine reaction surfaces/interfaces that form and the mechanisms that control reactivity. Silica-rich reaction layers and surface regions missing glasslike layer fragments were routinely observed (Figure 2), indicating reaction-layer formation, cracking, and exfoliation are integral to the carbonation process. As these layers are found to inhibit the

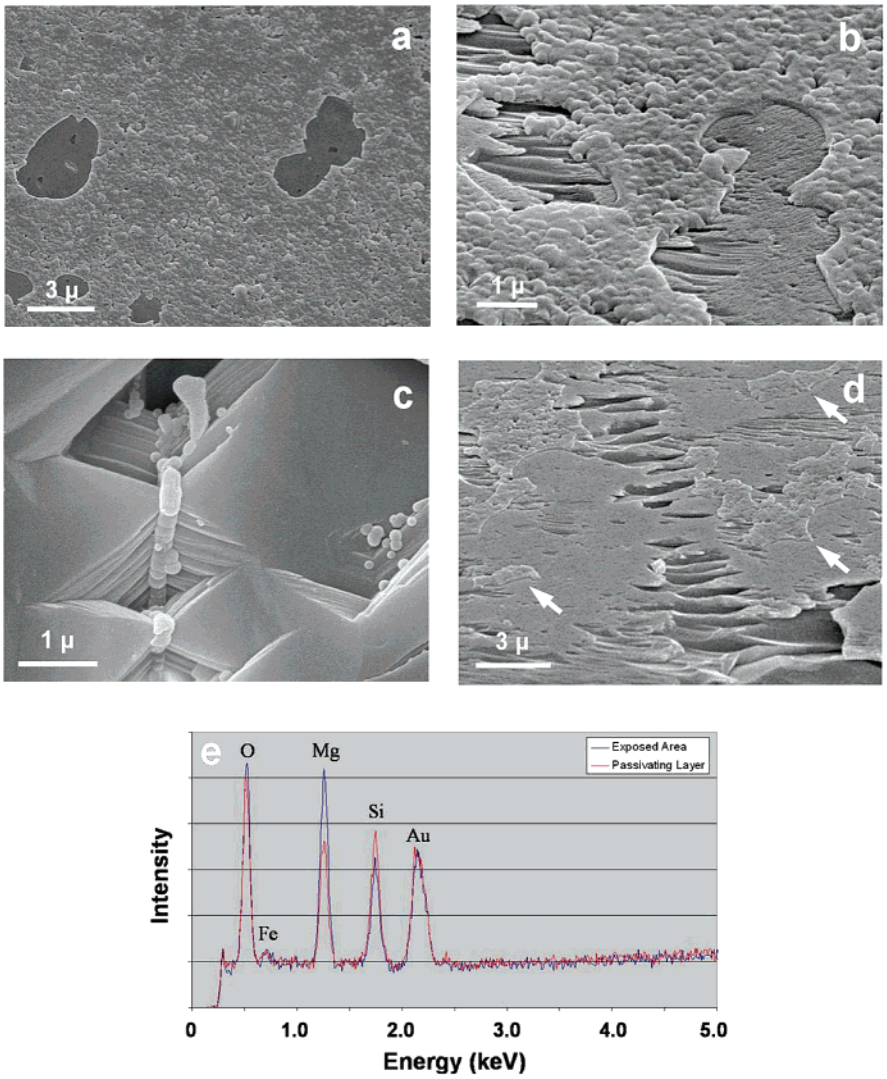

FIGURE 2. FESEM images of reaction surfaces formed during 1500 rpm stirred carbonation. (a) Silica-rich passivating layer showing regions that experienced fracture and exfoliation. (b) Regrowth of new layers in exfoliated regions. (c) Regions near etch pits were often devoid of passivating layers but occasionally show evidence of silica dissolution/precipitation. (d) Region that experienced passivating layer fracture, exfoliation, and regrowth. The exposed olivine surfaces appear associated with olivine defects. Note the olivine fragment that appears partially broken away (lower right). Passivating layer "island" remnants are indicated by white arrows. (e) EDS of the reaction surface shown in b. Analysis of the passivating layer and exposed olivine surfaces are shown by the red and blue curves, respectively. The sample is gold coated to minimize charging.

carbonation process, as discussed later, they are hereafter referred to as passivating layers. Figure 2b shows an area that has experienced glasslike fracture and exfoliation where new passivating layer regions have begun to regrow on the exposed olivine surfaces, highlighting that passivating layer growth, cracking, exfoliation, and regrowth occur repeatedly during carbonation. The silica-rich nature of the layers that form is evident in Figure 2e, which shows EDS spectra for passivating-layer and recently exfoliated (olivine exposed) regions. The thin silica-rich passivating layers that form reduce and increase the Mg and Si peak intensities, respectively, for the passivating-layer region observed as the EDS sampling depth includes both the passivating layer and some underlying olivine.

A small fraction of the surfaces observed (≤1%) were largely free of passivating layer formation. Surface irregularities, especially etch pits, were generally found in these regions (Figure 2c). This suggests defects such as dislocations, inclusions, and low-angle grain boundaries commonly found in San Carlos olivine (*10*) can significantly impact local carbonation reactivity by raising the olivine surface energy via strain field formation and lead to the locally enhanced congruent dissolution observed. Although passivating layers are not typically observed in these regions, irregular silica-rich deposits are occasionally found, suggesting they are largely associated with silica deposition (Figure 2c). The irregular surface morphology of the passivating layers is quite similar to that observed for individual silica particles as well as hydrothermally deposited silica (*13*), suggesting silica deposition may also occur on passivating layer surfaces. Figure 2d shows a region that has experienced passivating layer fracture, exfoliation, and growth/regrowth and exhibits exposed olivine surfaces. The fragment that appears partially broken away from the surface suggests the exposed surfaces may be associated with the breaking away of small olivine fragments during carbonation. Several independent passivating layer islands with glasslike fracture edges still remain after the particle has experienced substantial abrasion and exfoliation, indicating the layers are initially strongly bound to the olivine and consistent with incongruent olivine dissolution.

We are conducting a parallel investigation of the passivating layer/olivine interface using large, olivine single crystals reacted *without* stirring to avoid particle collisions

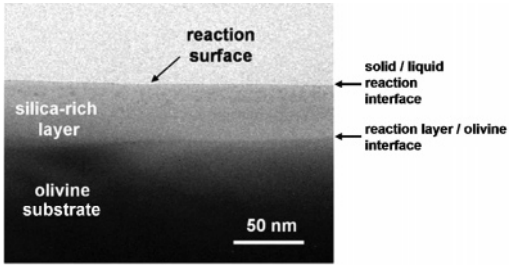

FIGURE 3. TEM cross-section image of the thin amorphous reaction layer that formed on the olivine single-crystal substrate early during unstirred carbonation.

eroding the layer that forms. Cross-section specimens are examined by high-resolution transmission analytical electron microscopy. Imaging and diffraction showed the passivating layer to be thin and amorphous; nanospectroscopy (electron energy loss and characteristic X-ray) showed the layer composition to be SiO_x with $x \leq 2$ (*15*). An example of the structure is shown in Figure 3. A small volume fraction of crystalline magnesite nanoparticles was also present in the layer with the layer best described as a dilute nanoparticle distribution in an amorphous ($\sim SiO_2$) matrix (*15*). The layer formed is highly stressed due to the large difference in molar volume between SiO_2 and olivine. Such stress can facilitate the passivating layer fracture and exfoliation observed during stirred carbonation.

Passivating layer formation appears to be a complex process that can be associated with incongruent dissolution and silica deposition on the reaction (e.g., passivating layer) surfaces that form. Hydrothermal deposition is known to be able to form brittle silica (*13*). Combined with the interfacial passivating layer/olivine stress associated with incongruent dissolution, the resulting passivating layers are expected to be highly susceptible to fracture and exfoliation, as observed.

Aqueous olivine dissolution is a complex process with a range of dissolution rates and incongruent as well as congruent dissolution observed as a function of pH and the presence of anionic species that can impact dissolution at the reaction surface (e.g., chelating agents, such as potassium acid phthalate, KHP) (*16*−*20*). To better ascertain the activities and pH during carbonation, solution equilibrium thermodynamics was analyzed using FactSage (v54) thermochemical modeling software (*21*). The Helgeson aqueous solution database was used with extended Debye−Huckel Davies activity coefficients. For the equilibrium solution calculations, the gas-phase CO_2 fugacity was fixed to the value obtained from the Duan et al. CO_2/H_2O equation of state for the same P_{CO2} and T conditions (*22*). Equilibrium aqueous speciation distribution and activities were obtained over a range of temperatures and P_{CO2} values for aqueous 1 M NaCl + 0.64 M $NaHCO_3$ and are similar to those previously reported (*7*). The pH was found to be 6.85 for $P_{total} = 150$ bar, where P_{CO2} is ~135 bar ($f_{CO2} \approx 115$ bar).

A currently accepted picture of olivine dissolution for pH < 9 under ambient conditions is based on the ion-exchange reaction $Mg^{2+} \Leftrightarrow 2H^+$ and formation of >SiOH groups (*16*, *17*). These groups can either condense to form oxide bonds within the reaction layer via

$$>Si{-}OH + HO{-}Si< \rightarrow >Si{-}O{-}Si< + H_2O$$

during incongruent dissolution or dissolve as $Si(OH)_4$ monomers that can later condense/polymerize and precipitate via >Si−O−Si< bonding and H_2O evolution (*14*, *16*−*20*). As the silica-containing samples observed in this study are largely H free (see above), it is reasonable to assume that >SiOH groups that form during carbonation are transitory, readily succumbing to >Si−O−Si< bonding to yield the brittle passivating layers observed. Indeed, the brittle fracture observed suggests substantial >Si−O−Si< bonding is present in the in-situ passivating layers that form. The formation of silica-rich layers (<20 Å thick) has been previously observed during ambient olivine dissolution for pH < 9 (*16*, *17*), suggesting the layers contain some permeability to the species associated with dissolution (e.g., Mg^{2+}, H^+, and H_2O).

Simulation of Passivating Layer Formation. Although the level of >Si−O−Si< bonding present in the passivating layers is not clear, our ex-situ observations show they are largely H free. Consequently, we simulated the anhydrous amorphous silica-rich layer to provide a plausible representation of the ex-situ anhydrous mineral surface investigated. A classical force field approach was applied to investigate the stability, structure, and permeability of siloxane passivating layer formation associated with incongruent dissolution. A 12 000 atom model that spans the region from within the olivine to the reaction region and the solution interface was used. The interaction between individual ions is represented by long-range coulomb interactions and short-range potentials consisting of an exponential repulsion and a van der Waals tail ("Born−Mayer" form).

Classical molecular dynamics simulations were carried out using the MOLDY computer program (*23*). The force fields employed are based on those developed for $MgSiO_3$ by Matsui (*24*) with slightly modified formal charges and Born−Mayer potential parameters for Mg and Si chosen to simultaneously reproduce the equations of state of α-quartz (SiO_2) and forsterite (Mg_2SiO_4). The pair potential parameters, given as pairs (A, b) for the repulsive part of the Born−Mayer form $V = Ae^{-br} - C/r^6$ are as follows: O−O (1.622, 3.333), Mg−O (8.038, 4.951), Si−O (7.367, 5.263), Mg−Mg (1301.1, 9.615), Mg−Si (2329.2, 10.87), and Si−Si (5008.1, 12.501), where the units are 10^{-3} eV and $Å^{-1}$, respectively. Only the O−O pair has a nonvanishing van der Waals C parameter, which is 30.22 eV $Å^6$. Ionic charges for O, Mg, and Si ions are −1.365, 1.365, and 2.730 e, respectively.

To benchmark our procedure we calculated the equilibrium volume of both α-quartz (SiO_2) and forsterite (Mg_2SiO_4) at 300 K over a pressure range of −20 to 80 GPa. The simulations of the basic crystalline phases were carried out in a supercell built from $N \times N \times N$ replicas of the respective unit cells ($N \approx 3$−6). All runs used an integration time step of 0.5 fs, velocity rescaling every 10 time steps, and between 10 000−100 000 time steps per run. The energy volume data was fitted to a standard Birch−Murnaghan equation of state form (*25*) to extract the equilibrium volume (V_0) and bulk modulus (B_0) at ambient pressure. For forsterite we obtained $V_0 = 69.3$ $Å^3$ and $B_0 = 121$ GPa (experimental values (*26*) $V_0 = 72.6$ $Å^3$, $B_0 = 123$ GPa), while for α-quartz we obtained $V_0 = 39.1$ $Å^3$ and $B_0 = 40$ GPa (experimental values (*26*) $V_0 = 37.2$ $Å^3$, $B_0 = 37$ GPa). To further calibrate our procedure and test the ability of the pair potentials to describe amorphous systems we undertook a brief study of silica glass. A structural model was obtained by melting a 648-atom cell of α-quartz and quenching from 3000 K by simulated annealing in nine 300 K cooling stages of 80 000, 0.5 fs time steps. The resulting structure exhibits all of the hallmarks of thermal glass, including a fully connected corner-shared tetrahedral SiO_4 network, and a mean density of about 2.31 g/cc, which is slightly high compared with the experimental value of ~2.20 g/cc. To further quantify the bonding distribution of the simulated glass we computed the radial distribution function and found it closely reproduces the essential structure observed by neutron scattering for annealed silica glass (Figure 4a,b) (*27*).

As the dissolution rates associated with passivating layer (PL) growth via incongruent dissolution are beyond the reach of our simulation times, we devised a synthetic procedure to simulate the low-temperature process. Beginning with a

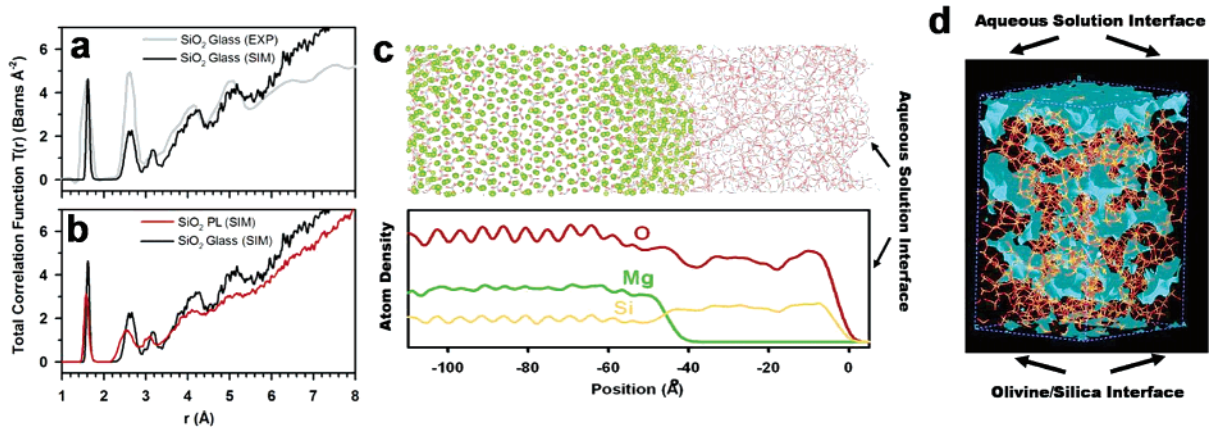

FIGURE 4. (a) Total correlation function of SiO_2 glass obtained from neutron scattering experiments (*27*) (gray trace) and molecular dynamics simulation (black trace). (b) Comparison of the total correlation function of simulated SiO_2 glass (black trace) and PL silica (red trace). (c) Simulated forsterite/passivating layer reaction interface and its atom density vs distance from the aqueous solution interface. Mg, O, and Si atoms correspond to green spheres, red sticks, and gray sticks, respectively. The variation of Mg, O, and Si atoms throughout the structure is plotted in the frame below the model. Note that the apparent densification of Mg atoms near −50 Å is due to the projection employed, which emphasizes the departure from periodic crystalline order in the transition region (ca. −65 to −40 Å). (d) PL regions that can accept a 4 Å probe without making van der Waals contact (shown in blue). The presence of continuous permeable regions can facilitate reactant species diffusion in and through the PL.

large forsterite slab, we randomly remove Mg and O atoms from the outermost region, 10 Å at a time, and then carry out a brief relaxation run to re-equilibrate the defective structure without promoting significant Mg diffusion. We continue this process until Mg on one-half of the full slab is removed. A final annealing run at 500 K is performed, leading to diffusion of Mg and formation of a reaction interface approximately 20 Å in thickness and an ∼50 Å PL with approximately SiO_2 stoichiometry (Figure 4c). Substantial contraction of the newly formed silica region relative to its extent in the olivine framework was observed. The PL formed consists of a low-density glasslike SiO_2 network with bonding very similar to thermal SiO_2 glass (O:Si ratio close to 2). The layer formed is thermally stable, remaining essentially unchanged during heating/cooling cycles from 300 to 600 K. The RDF of the PL material is compared with that of the simulated bulk silica glass in Figure 4b. The results indicate a marked change in medium-range order, consistent with a slight reduction in first shell coordination and the presence of ring structures.

Layer permeability is critical for PL formation via incongruent dissolution as it facilitates both the transport of Mg ions through the layer and formation of water and its expulsion from the layer. Close examination of the simulated PL structure suggests it may be permeable to key species associated with mineral carbonation (e.g., Mg^{2+}, H^+, and H_2O), consistent with incongruent dissolution. Such permeability does not exist in our quenched thermal SiO_2 glass model but does for the simulated PL structures. Interestingly, the RDFs calculated for the simulated SiO_2 glass and PL material have significant similarities, suggesting very similar short-range structures (Figure 4b). To reveal the differences between the structures we appeal to a "free volume" analysis module available in the Cerius2 simulation software suite (*28*). The occupiable volume is probed by overlaying grid points set at 0.5 Å intervals throughout the structure. A probe particle is sequentially placed at each grid point with the point considered "occupiable" if there is no van der Waals contact with the PL structure in any of several hundred directions. Nine probe particles with diameters ranging from 2 to 6 Å were used. As expected on the basis of visual inspection and density, the strained PL structure, which was relaxed while bonded to the host olivine, exhibits the largest fractional occupiable volume. This is followed by the relaxed PL structure, which is first severed at the olivine interface and then relaxed as above, and thermal glass. About 7% of the occupiable volume of the strained PL material was found to be able to accommodate H_2O molecules ($\mathbf{D}_{probe} \approx 2.8$ Å) (*29*), while about 5% of the volume can accommodate H_2O in the relaxed PL material (even using the 2 Å probe, the occupiable volume in thermal glass is negligible). Slightly greater occupiable volumes are expected for Mg^{2+} owing to its smaller diameter. To explore the potential impact of the strained and relaxed PL structures on the diffusion of the species associated with mineral carbonation, the regions of the PL that can accept different probe diameters were mapped out. Their interconnection, as illustrated in Figure 4d, suggests plausible diffusion pathways for reactant species within the PL produced during incongruent dissolution.

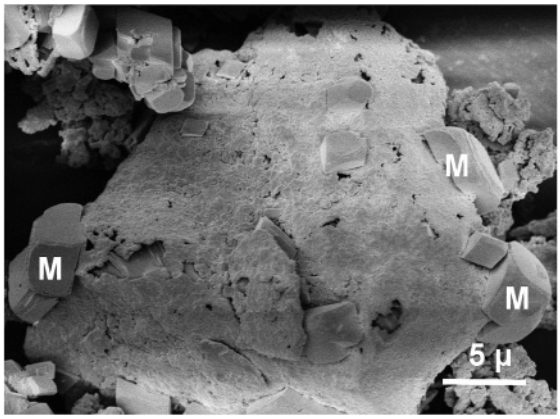

FIGURE 5. FESEM image of the intergrowth between olivine, silica, and magnesite at the olivine reaction surface. Selective abrasion of the outer magnesite (M) crystal surfaces indicate the composite particle formed during stirred carbonation.

Intergrowth of Carbonate, Silica, and Olivine During Aqueous Carbonation. Intergrowths of olivine, magnesite, and silica were also observed on the surface of partially carbonated particles, as seen in Figure 5. Selective erosion of the outside corners of surface magnesite crystals was routinely observed, confirming (i) significant particle abrasion occurs during carbonation and (ii) the observed olivine/silica/magnesite intergrowth formed during carbonation and not via precipitation or particle settling after reaction completion. Figure 6 shows cross-section analysis of a similar partially reacted crystal, which illustrates the inward progression of

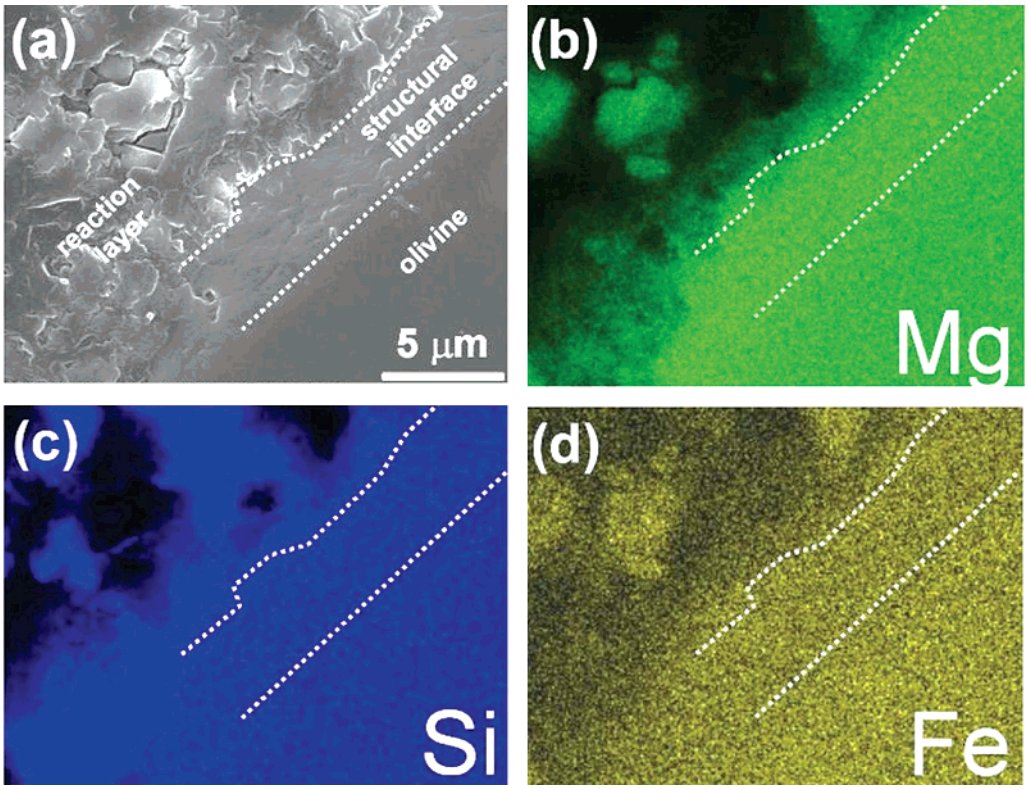

FIGURE 6. (a) FESEM secondary electron image of a cross-section of a partially carbonated olivine single crystal showing structural disruption of the olivine preceding carbonation as the reaction penetrates to the crystal interior. The crystal surface is in the upper left corner. (b–d) Mg, Si, and Fe EDS maps of the region in a.

the reaction from the olivine surface during stirred carbonation. The olivine near the reaction layer interface appears structurally disrupted (e.g., cracked) *prior to* reaction penetration, which may be related in part to volume contraction associated with silica-rich passivating layer formation via incongruent dissolution at the olivine reaction interface. This observation underscores the key role structural disruption can play in enhancing carbonation reactivity, especially given how effective silica layer formation can be at local reaction passivation. In this case, some magnesite is observed in the silica reaction layer, as evidenced by the separate Si- and Mg-rich regions in the layer observed by EDS. The strong correlation between Mg and Fe in the olivine feedstock and the magnesite in the reaction layer (Figure 6) indicates Fe is also incorporated into the carbonate during carbonation. The silica regions observed are essentially Fe free.

Controlled Particle Abrasion: Enhancing Passivating Layer Exfoliation and Carbonation. Silica-rich passivating layer formation during mineral carbonation clearly has the potential to substantially inhibit carbonation reactivity. However, the layers that form are brittle, strained, and susceptible to fracture and exfoliation that can expose fresh olivine surfaces that enhance reactivity. Hence, particle interactions may significantly enhance carbonation reactivity. To probe the potential particle–particle interactions (abrasion) offer to erode passivating layers as they form and enhance reactivity, we investigated the extent of carbonation vs wt % forsterite for stirred (1500 rpm) carbonation, as seen in Figure 7. The systematic increase in the extent of carbonation with increasing wt % forsterite (particle concentration) demonstrates (1) the importance of particle–particle interactions (abrasion) in exposing fresh olivine reaction surfaces and enhancing carbonation and (2) that the observed silica-rich surface layers substantially inhibit (passivate) carbonation. In recent simulations of colliding monodisperse spheres in forced isotropic turbulent flow, corresponding closely to the stirred tank conditions in our

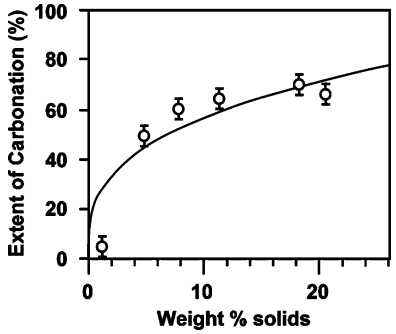

FIGURE 7. Extent of carbonation vs wt % forsterite. The error bars show the standard deviation typically observed for multiple runs under the same reaction conditions. The gray line is a fit to the form $AW^{1/3}$, where $A \approx 26.2$. (We note that the assumed functional form is only expected to be valid in the absence of particle agglomeration, which is expected to be significant in higher wt % solid regimes).

experiments, Derksen et al. (*30*) identified two distinct collision mechanisms: (i) primary collisions consisting of uncorrelated "kinetic gas"-like random contacts and (ii) highly correlated secondary collision processes involving repetitive "chattering" motion on a short time scale due to short-range hydrodynamic effects (lubricating forces). Elementary geometric considerations deliver a length scale (L) dependence on wt % solids, W, proportional to $W^{1/3}$. The removal rate of PL material, R_{PL}, is therefore proportional to $V_{avg}/L = AW^{1/3}$, where V_{avg} is the mean relative velocity between a pair of particles and A is a constant. If we assume that the diffusion of reactants through the PL is rate limiting and that complete passivation occurs in a time T_0 in an unstirred setting, then the extent of carbonation is proportional to $T_{RUN}\,R_{PL} \propto W^{1/3}$ where $T_{RUN} \gg T_0$ is the duration of the stirred reaction experiment. This dependence on wt % solids is illustrated in Figure 7, where a best fit yields a

proportionality constant of about 26.2, a value much larger than expected based on primary collisions alone. The large coefficient may be explained by a high frequency of secondary collision processes.

We recently discovered the inclusion of abrasive particles (e.g., quartz) leads to a marked increase in carbonation. This indicates controlling particle abrasion by optimizing slurry flow parameters may provide an effective mechanism for disrupting passivating layers as they form. The effective use of larger feedstock particles may promote this effect and substantially lower sequestration process cost as the vast majority of the cost in grinding the olivine feedstock to the current process size (<37 μm) is associated with particle-size reduction from <75 to <37 μm (*9*).

Acknowledgments

This work was prepared with the support of the U.S. Department of Energy, under Award No. DE-FG26-04NT42124. However, any opinions, findings, conclusions, or recommendations expressed herein are those of the author(s) and do not necessarily reflect the views of the DOE. We also gratefully acknowledge the National Energy Technology Laboratory of the U.S. Department of Energy for prior support through Awards DE-FG26-01NT41282 and DE-FG26-01NT41295 and thank the Center for Solid State Science for use of the Goldwater Materials Science Laboratories, including the Materials and Ion Beam Facilities and the Goldwater Materials Visualization Facility. We acknowledge the Department of Chemistry and Biochemistry for use of the X-ray Diffraction and Microprobe Facilities and the Center for Solid State Electronics Research for use of the FESEM.

Literature Cited

(1) *Novel Approaches to Carbon Management*; National Academies Press: Washington, DC, 2003.
(2) Lackner, K. S. Carbonate chemistry for sequestering fossil carbon. *Annu. Rev. Energy Environ.* **2002**, *27*, 193.
(3) Halmann, M.; Steinberg, M. *Greenhouse Gas Carbon Dioxide Mitigation, Science and Technology*; Lewis Publishers: London, 1999.
(4) Seifritz, W. CO_2 Disposal by means of silicates. *Nature* **1990**, *345*, 486.
(5) Lackner, K.; Wendt, C.; Butt, D.; Joyce, E., Jr.; Sharp, D. Carbon dioxide disposal in carbonate minerals. *Energy* **1995**, *20*, 1153.
(6) O'Connor, W. K.; Walters, R. P.; Dahlin, D. C.; Rush, G. E.; Nilsen, D. N.; Turner, P. C. Carbon dioxide sequestration by direct aqueous mineral carbonation. *Proc. 26th International Technical Conference on Coal Utilization & Fuel Systems* **2001**, 765.
(7) Wolf, G. H.; Chizmeshya, A. V. G.; Diefenbacher, J.; McKelvy, M. J. In situ observation of CO_2 sequestration reactions using a novel microreaction system. *Environ. Sci. Technol.* **2004**, *38*, 932.
(8) McKelvy, M. J.; Chizmeshya, A. V. G.; Diefenbacher, J.; Béarat, H.; Wolf, G. H. Exploration of the role of heat activation in enhancing serpentine carbon sequestration reactions. *Environ. Sci. Technol.* **2004**, *38*, 6897.
(9) O'Connor, W. K.; Dahlin, D. C.; Rush, G. E.; Gerdemann, S. J.; Penner, L. R. Energy and economic considerations for ex situ aqueous mineral carbonation *Proc. 29th International Technical Conference on Coal Utilization & Fuel Systems* **2004**, 71.
(10) Johnson, C. L.; Hytch, M. J.; Buseck, P. R. Displacement and strain fields around a [100] dislocation in olivine measured to sub-angstrom accuracy. *Am. Mineral.* **2004**, *89*, 1374. *Electron Microscopy in Mineralogy*; Wenk, H., Ed.; Springer-Verlag: Berlin, 1976; Chapters 6.1 and 6.6.
(11) Hurlbut, C. S.; Klein, C. *Manual of Mineralogy*, 19th ed.; John Wiley & Sons: New York, 1977.
(12) Ottonello, G.; Princivalle, F.; Della Giusta, A. Temperature, composition, and fO2 effects on intersite distribution of magnesium and iron(2+) in olivines. Experimental evidence and theoretical interpretation. *Phys. Chem. Miner.* **1990**, *17*, 301.
(13) Potapov, V. V. Formation of Solid Deposits of Amorphous Silica in a Flow of Hydrothermal Solution. *Glass Phys. Chem.* **2004**, *30*, 82.
(14) Weissbart, E. J.; Rimstidt, J. D. Wollastonite: Incongruent dissolution and leached layer formation. *Geochim. Cosmochim. Acta* **2000**, *64*, 4007.
(15) Kim, Y.; Nunez, R.; Carpenter, R. W.; Chizmeshya, A. V. G.; McKelvy, M. J. The nanoscale mechanism for San Carlos olivine carbonation *Microsc. Microanal.* **2005**, *11* (Suppl 2), 1530.
(16) Pokrovsky, O. S.; Schott, J. Forsterite surface composition in aqueous solutions: A combined potentiometric, electrokinetic, and spectroscopic approach. *Geochim. Cosmichim. Acta* **2000**, *64*, 3299.
(17) Pokrovsky, O. S.; Schott; J. Kinetics and mechanism of forsterite dissolution at 25 °C and pH from 1 to 12. *Geochim. Cosmichim. Acta* **2000**, *64*, 3313.
(18) Wogelius, R. A.; Walther, J. V. Olivine dissolution at 25 °C: effects of pH, CO_2, and organic acids. *Geochim. Cosmichim. Acta* **1991**, *55*, 943.
(19) Jonckbloedt, R. C. L. Olivine dissolution in sulphuric acid at elevated temperatures−implications for the olivine process, an alternative waste acid neutralizing process. *J. Geochem. Explor.* **1998**, *62*, 337.
(20) Chen, Y.; Brantley, S. L.; Dissolution of forsteritic olivine at 65 °C and 2<pH<5 *Chem. Geol.* **2000**, *165*, 267.
(21) Bale, C. W.; Chartrand, P.; Decterov, S. A.; Eriksson, G.; Hack, K.; Mahfoud, R. B.; Melançon, J.; Pelton, A. D.; Petersen, S. FactSage Thermochemical Software and Databases. *Calphad J.* **2002**, *62*, 189.
(22) Duan, Z.; Moller, N.; Weare, J. H. An equation of state for the CH_4–CO_2–H_2O system: II. Mixtures from 50 to 1000C and 0 to 1000bar *Geochim. Cosmochim. Acta* **1992**, *56*, 2619.
(23) Refson, K. *Moldy User's Manual*, Rev. 2.25.2.6, release 2.16; Department of Earth Sciences: Oxford, United Kingdom, 2001.
(24) Matsui, M. Molecular dynamics study of $MgSiO_3$ perovskite. *Phys. Chem. Miner.* **1988**, *16*, 234.
(25) Birch, F. Finite Strain isotherm and velocities for single-crystal and polycrystalline NaCl at high pressures and 300 K. *J. Geophys. Res.* **1978**, *83*, 1257.
(26) Knittle, E. *Mineral Physics and Crystallography: A Handbook of Physical Constants*; Ahrens, T. J., Ed.; American Geophysical Union: Washington, DC, 1995; Vol. 2, p 98.
(27) Johnson, P. A. V.; Wright, A. C.; Sinclair, R. N. Neutron scattering from vitreous silica II. Twin-axis diffraction experiments. *J. Non-Cryst. Solids* **1983**, *58*, 109.
(28) *Cerius2 Simulation Program*; Accelrys Inc.: San Diego, CA, 2003.
(29) Franks, F. *Water: A matrix of life*, 2nd ed.; Royal Society of Chemistry: Cambridge, 2000.
(30) Cate, A. T.; Derksen, J. J.; Portela, L. M.; van den Akker, H. E. A. Fully resolved simulations of colliding monodisperse spheres in forced isotropic turbulence. *J. Fluid Mech.* **2004**, *519*, 233.

Received for review November 18, 2005. Revised manuscript received March 23, 2006. Accepted May 5, 2006.

ES0523340